NONCONTACT NONLINEAR RESONANCE ULTRASOUND SPECTROSCOPY FOR SMALL METALLIC SAMPLES

A Thesis
Presented to
The Academic Faculty

by

Steffen Maier

In Partial Fulfillment
of the Requirements for the Degree
Master of Science in Engineering Science and Mechanics in the
School of Civil and Environmental Engineering

Georgia Institute of Technology
December 2017

NONCONTACT NONLINEAR RESONANCE ULTRASOUND SPECTROSCOPY FOR SMALL METALLIC SAMPLES

Approved by:

Professor Laurence J. Jacobs, Advisor
School of Civil and Environmental Engineering
Georgia Institute of Technology

Dr. Jin-Yeon Kim
School of Civil and Environmental Engineering
Georgia Institute of Technology

Dr. Jianmin Qu
G.W. Woodruff School of Mechanical Engineering
Georgia Institute of Technology

Date Approved: 11 August, 2017

ACKNOWLEDGEMENTS

First and foremost, I want to deeply thank my advisor Professor Laurence J. Jacobs for his constant support and making it possible for me to come to Georgia Tech. His advice kept me motivated and focused throughout my graduate studies and I am grateful for having the opportunity to participate in the quantitative nondestructive evaluation (QNDE) conference in Provo, Utah. I was always looking forward and enjoying our frequent pizza evenings and ice cream runs with the whole lab. Larry, you truly made it an amazing time that I will never forget.

Furthermore, I want to thank Dr. Jin-Yeon Kim for the many interesting and enlightening conversations and his invaluable practical and professional advice that guided me throughout my research. I really enjoyed the unconstrained atmosphere in the lab and the academic freedom I had.

I also would like to thank Dr. Joe Wall of the Electric Power Research Institute (EPRI) for his insights and contributions.

Thank you to my lab mates Katie Scott, Gun Kim, David Torello, Brian Fuchs, Miralem Saljanin and Timm Geibel for making the time in the lab interesting, productive and at the same time entertaining. My special thanks thereby goes to Miralem and Timm together with the other housemates of Terrell Street for sharing joy and sorrow and making it a truly unforgettable time in Atlanta.

I would also like to express my gratitude to Prof. Michael Hanss, Dennis Schurr and Christian Ehrlich of the University of Stuttgart for choosing me as a candidate for this program and giving me the opportunity to study at Georgia Tech. Also I would like to thank the German Academic Exchange Service (DAAD) for providing generous financial support for my studies in the U.S.

Last but not least I would like to express my deepest gratitude to my family and Franziska for supporting and motivating me throughout my time in Atlanta.

TABLE OF CONTENTS

LIST OF TABLES

LIST OF FIGURES

LIST OF SYMBOLS AND ABBREVIATIONS

Abbreviations

Abbreviation	Description
AC	Air Cooled
EDM	Electrical Discharge Machining
FFT	Fast Fourier Transformation
GQ	Gas Quenched
LDV	Laser Doppler Vibrometer
NEWS	Nonlinear Elastic Wave Spectrocopy
NRS	Nonlinear Reverberation Spectroscopy
NRUS	Nonlinear Resonant Ultrasonic Spectroscopy
PH	Precipitate-Hardened
RUS	Resonance Ultrasonic Spectroscopy
RPV	Reactor Pressure Vessel
SHG	Second Harmonic Generation
TEP	Thermo-Electric Power

Latin Symbols

Symbol	Description
c	Speed of sound, phase speed
E	Young's modulus
f	Frequency
F	Force
f_0	Equilibrium resonance frequency
Δf	Frequency shift
Δf_{hp}	Half-power bandwidth

f_c	Cut-off frequency
f_{exp}	Experimentally determined natural frequency
f_{sim}	Simulative determined natural frequency
k	Wave number
k_h	Flare constant
k_x, k_y, k_z	Spring constant per unit length respective to coordinate axis
K	Nonlinear and hysteretic modulus
K_0	Linear modulus
L	Sample length
L_c	Length of hysteretic element in closed state
L_I	Distance between impurities
L_N	Network length
L_o	Length of hysteretic element in opened state
Q	Quality factor
Q_{exp}	Experimentally determined quality factor
R^2	Coefficient of determination
S	Cross-sectional area
r	Cross-sectional radius
t	Time
S	Seebeck coefficient
T	Temperature
T_l	Longitudinal wave transmission coefficient
u	Displacement
U	Displacement amplitude
v	Velocity
v_{max}	Maximal velocity
Z	Acoustic impedance

Greek Symbols

Symbol	Description
α	Hysteretic nonlinearity parameter
α'	Relative hysteretic nonlinearity parameter
β	Acoustic (first order classical) nonlinearity parameter
β'	Relative acoustic nonlinearity parameter
δ	Second order classical nonlinearity parameter
ϵ	Strain
ϵ_{dis}	Dislocation strain
$\dot{\epsilon}$	Strain rate
$\Delta\epsilon$	Strain amplitude
ρ	Density
ν	Poisson's ratio
σ	Stress
σ_c	Stress in hysteretic element in closed state
σ_o	Stress in hysteretic element in open state
ω	Angular frequency

SUMMARY

The aim of this research is to evaluate the influence of microscopic material damage to the hysteretic nonlinearity parameter, α. Therefore, this study applies contact and noncontact setup combinations of the nonlinear resonance ultrasound spectroscopy (NRUS) technique to small metallic specimen and analyzes their validity and significance.

The various resonance modes of small plates (20 mm x 1 mm) and slender bars (10 mm x 10 mm x 100 mm) are excited by contact-coupled and noncontact air-coupled piezoelectric transducers and a laser vibrometer detects the out-of-plane velocity of the vibrating specimen surfaces. The amount of the shift of the resonance frequency for increasing excitation levels represents the nonlinear behavior of the material. The experimental setups together with the measuring and data processing protocols are optimized and analyzed for measurement accuracy and system nonlinearity and evaluated with the results of a thermally aged 17-PH stainless steel measurement series.

The results show the advantages of noncontact over contact excitation and demonstrate the sensitivity of this NRUS technique to microstructural changes in stainless steel.

CHAPTER I

INTRODUCTION

1.1 Motivation

Nondestructive evaluation (NDE) has proven to be a powerful tool to achieve high levels of security and reduce maintenance costs in a variety of branches. Especially application areas with very high safety standards such as aerospace, transportation, civil engineering and energy production, here in particular when nuclear technology is involved, employ a variety of nondestructive techniques to assess material damage and conditions. Since many nuclear reactors in the US and abroad are reaching their original design operation time the needs for monitoring irradiation damage will be particularly in great demand.

More conventional and commonly used linear ultrasonic techniques are capable of detecting macroscopic damage such as cracks and cavities or determining stiffness parameters, but are less sensitive to evenly distributed degradation and material features that are orders of magnitude smaller than the wavelength of the ultrasonic wave. This limits the capabilities to detect microstructural changes in the material that occur during processes like deformation, thermo damage, creep, fatigue, nuclear irradiation and more that are below the order of the ultrasonic wavelength.

In addition, nonlinear ultrasonic techniques have shown shown great potential to monitor those microstructural changes that are orders of magnitude smaller than the ultrasonic wavelength by analyzing effects due to nonlinear elasticity. These techniques include higher harmonic generation, sub-harmonic generation, mixed frequency response and shift of resonance frequency [15]. Especially measurements of

the resonance frequency are well suited for small specimens and have a variety of advantages such as fast measurements with the potential of a high degree of automation and minimal sample preparation effort [12].

While resonance ultrasound spectroscopy (RUS), the linear variation of the resonance technique is becoming increasingly attractive to structural and machine component manufacturers [6] it is still very limited in sensitivity to early stages of damage development [32]. However, the nonlinear resonance ultrasound spectroscopy (NRUS) technique, that exploits nonlinear elasticity effects through determination of the material properties for increasing excitation, has shown capability of detecting internal degradation of the microstructural properties of the material. Contrary to these promising aspects of NRUS the technique is also very sensitive to influencing factors such as ambient temperature and humidity or bonding quality of glued on emitters and receivers and is very susceptible to precision deviation [13].

1.2 Objectives

The objective of this research is to use the NRUS technique and develop a reliable, accurate and valid method to measure the hysteretic nonlinearity parameter, α, of metallic specimens. This goal includes that on the basis of previous work from Forstenhäusler [8], the experimental setup is changed to variations of contact and non-contact excitation with great interest on the effect of setup components, mechanical conditions and ambient factors.

The method should be suitable for relatively small specimen sizes and should allow extensive measurement series with minimal sample preparation and fast measurement procedure with need of few repetitions. Furthermore, the experimental procedure should be operator-independent and as far as possible automated.

The developed NRUS measurement method should then prove its sensitivity to

changes in the microstructure of steel on the example of different stages of precipitation formation in 17-4 PH stainless steel, evaluated on the basis on previous complementary measurements on the same samples.

1.3 Structure of Thesis

After providing a general introduction to nondestructive evaluation techniques and introducing the objectives for this work in the first chapter, the following chapter gives a brief introduction into the nonlinear elasticity and its classification and a theoretical background to the NRUS measurement technique. Chapter 3 describes the properties, the applied heat treatment and resulting conditions of the material samples used for the contact and noncontact based measurement setups.

In chapters 4 and 5 these experimental setups, their included components and signal processing steps are explained and compared to a finite-element modal analysis model. The NRUS results for different materials and the heat treated 17-PH specimens are evaluated in aspects of validity and significance and put into context to complementary measurement techniques applied to the samples, eventually leading to the improvements between the two setups.

Finally, a further summary of the major findings and the conclusion with outlook to future work based on this research is provided in chapter 6.

CHAPTER II

THEORETICAL BACKGROUND

2.1 Nonlinear Elasticity

Nonlinear elastic behavior appears when a linear relationship between stress and strain, known as Hooke's law, no longer applies. For the precise description of the static and dynamic elastic behavior of most solids nonlinear terms in the stress-strain relationship are required. Such a formulation of the stress-strain relationship that includes nonlinear effects with different mechanisms and orders is given by the constitutive equation

$$\sigma = \int K(\epsilon, \dot{\epsilon})\, d\epsilon \tag{1}$$

with the nonlinear and hysteretic modulus

$$K(\epsilon, \dot{\epsilon}) = K_0 \left\{1 - \beta\epsilon - \delta\epsilon^2 - \alpha\left[\Delta\epsilon + \epsilon(t)\,\mathrm{sign}(\dot{\epsilon})\right] + ...\right\}, \tag{2}$$

where K_0 is the linear modulus, β and δ are the quadratic and cubic classical nonlinearity parameters, α is the hysteretic nonlinearity parameter, $\Delta\epsilon$ is the local strain amplitude and $\dot{\epsilon}$ is the strain rate with the sign function of the strain rate, sign($\dot{\epsilon}$) [30].

A schematic overview of the stress to strain relationship shapes of the linear and nonlinear parameters and their classification is given in Figure 1. The classical theory consists foremost of the linear or Hookian contribution and includes further the quadratic (or acoustic) nonlinearity parameter, β, and the cubic nonlinearity parameter, δ. Nonclassical nonlinear elastic effects that are not explained by the classical theory of elasticity have hysteretic character, involve energy dissipation for dynamic elasticity and are quantified by the nonclassical hysteretic parameter, α.

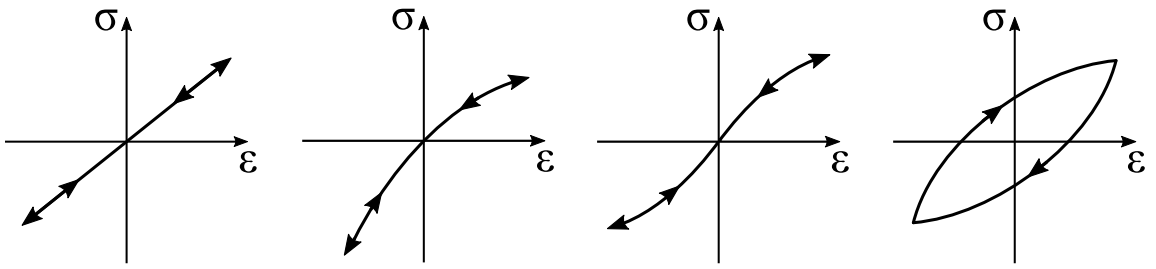

(a) Linear relationship K_0 (b) 1^{st} order classical nonlinearity β (c) 2^{nd} order classical nonlinearity δ (d) Nonclassical hysteretic nonlinearity α

Figure 1: Overview of the nonlinearity parameters contributing to the constitutive equation, adopted from Van Den Abeele et al. [30, Fig. 1]

Classical nonlinearity mainly depends on the crystalline structure of the material and local strain fields on an atomic level caused by anharmonicity of the interatomic potential, dislocations, precipitates or microcracks [20] [13]. Many theoretical models for material damage such like dislocation pinning, dislocation dipoles, precipitates and microcracks, contributing to classic crystal lattice nonlinearity have already been developed [18].

Nonclassical nonlinearity with hysteretic character and quasi-static discrete memory involving energy dissipation was first observed for materials of the mesoscopic-elasticity class such as rock, concrete or sandstone. Remarkably large hysteretic behavior, even for small strain levels, was measured for macro-defects and localized damage. Recent research states that these effects are due to soft regions in hard materials, detectable even on a much smaller scale, caused by microcracks, pores and soft bonding regions between material grain [1].

A phenomenological model to describe the hysteretic behavior and discrete memory effect of materials of the mesoscopic-elasticity class is the Preisach-Mayergoyz (P-M) space model. This model represents the material as a connection of many hysteretic elements. Each single element has two states as shown in Figure 2. In the closed state the element has the length L_c that increases to L_o for the open state, depending on the applied element stresses σ_c and σ_o. The P-M space is then described

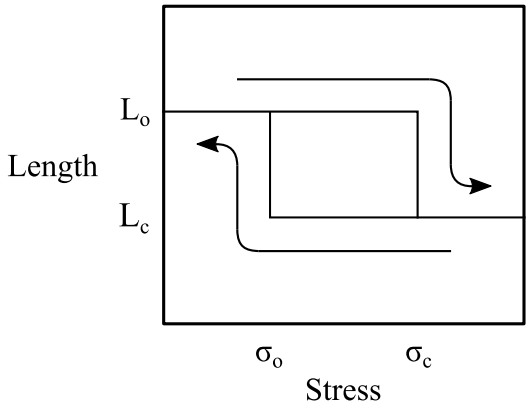

Figure 2: Hysteretic element (adopted from Guyer and Johnson [11])

with the stress properties of the elements as its coordinates as illustrated in Figure 3. From the equilibrium open state 0 to a half closed state A, the elastic element closes from left to right, following the lower hysteretic curve.

After being fully closed in state B the element opens again from top to bottom following the upper hysteretic curve reaching state A'. For the corresponding points A and A' the stress is the same, but the element is in a different elastic state, resulting in different strains. An explanation for the discrete memory effect is illustrated by

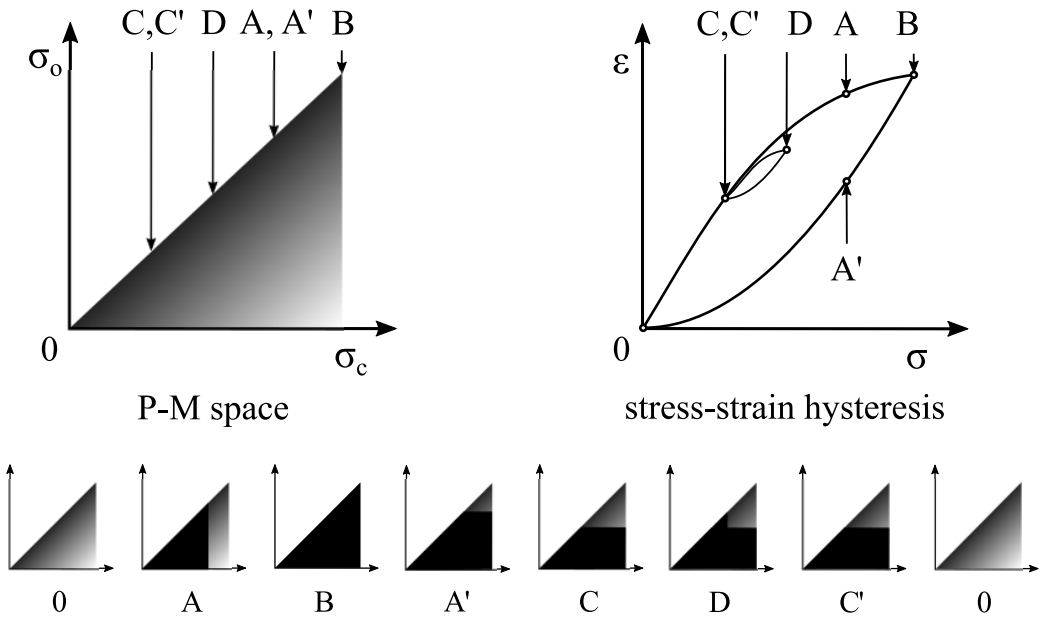

Figure 3: P-M space with element stresses and resulting stress-strain hysteresis protocol (adopted from Guyer and Johnson [11])

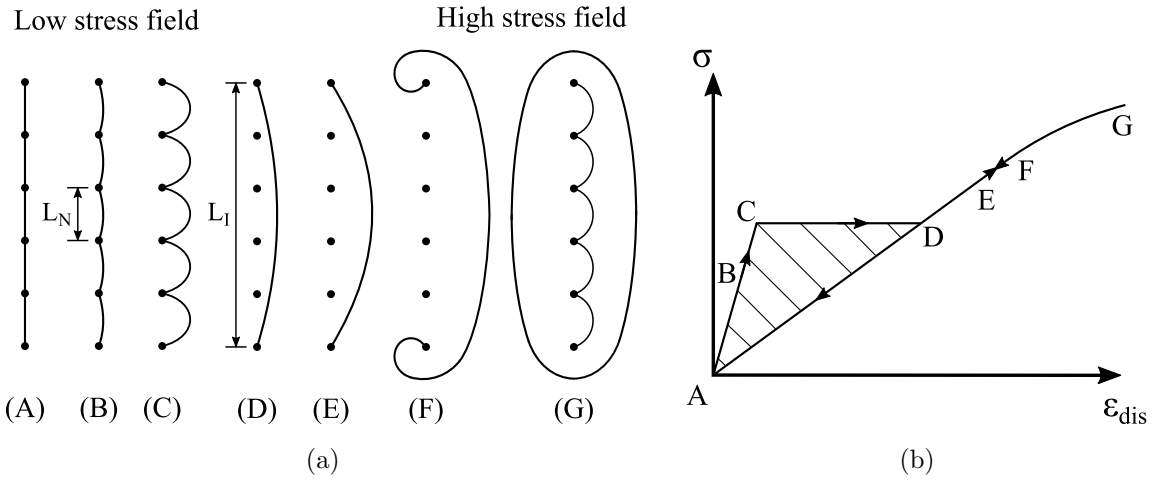

Figure 4: (a) Schematic model of an aligned dislocation network with dislocation line bowing out under increased applied pressure and (b) corresponding stress-dislocation strain protocol (adopted from Granato and Lücke [10, Fig. 1 and 2])

the smaller hysteresis loop from state C to D to C' [11].

A quantitative theory to describe damping and modulus changes in metals due to dislocations to explain hysteresis of crystal materials is given by Granato and Lücke [10]. Their model characterizes a crystal material in networks of aligned enclosed impurities with the network length L_N and distance L_I in between impurities. Due to the dislocations an applied external stress causes, additional to the elastic strain, a so-termed dislocation strain with a frequency dependent stress-dislocation law, constant for a low kilohertz range. Figure 4(a) illustrates from left to right increasing applied stress onto the dislocation line, causing it to continuously bow out from step (A) to (C) with linear modulus. The dislocation line breaks out from (C) to (D), where the stress stays the same, but the dislocation strain increases, pointed out by stress-dislocation strain relationship protocol in Figure 4(b). For steps (D) to (F) the bowing out process continues again with proportional stress-dislocation strain relation, now determined by L_N, finally leading to an irreversible detachment and formation of a closed dislocation loop. Hysteretic losses appear in this model because the stress relaxation from (D) to (A) is elastic along the modulus, determined by the network length, with a loss proportional to the enclosed area of the hysteresis loop. Granato

and Lücke further describe an additional frequency dependent dynamic loss caused by a phase lag for oscillating stress, largest close to resonance frequency and disappearing for low and high frequencies.

Observed nonlinear elastic behavior of materials of the atomic-elasticity class [7] [13] currently lack in theoretical models describing nonlinear elastic hysteretic effects on an atomic level. Hence it is often traced back to a mesoscopic level [9].

2.2 Nonlinear Resonance Ultrasound Spectroscopy

Nonlinear Resonance Ultrasound Spectroscopy (NRUS) is one technique of a group of nonlinear ultrasonic methods denoted Nonlinear Elastic Wave Spectrocopy (NEWS) that measures parameter changes for increasing excitation amplitude such as resonance frequencies, attenuation, fundamental frequencies and amplitudes of higher harmonics [2]. The NRUS technique, an extension of linear Resonance Ultrasonic Spectroscopy (RUS) that merely measures the equilibrium resonance frequency of a specimen to determine its stiffness parameters, examines the nonlinear vibrational response and evaluates the dependence of excitation amplitude to natural frequency, eventually determining nonlinear material hysteresis.

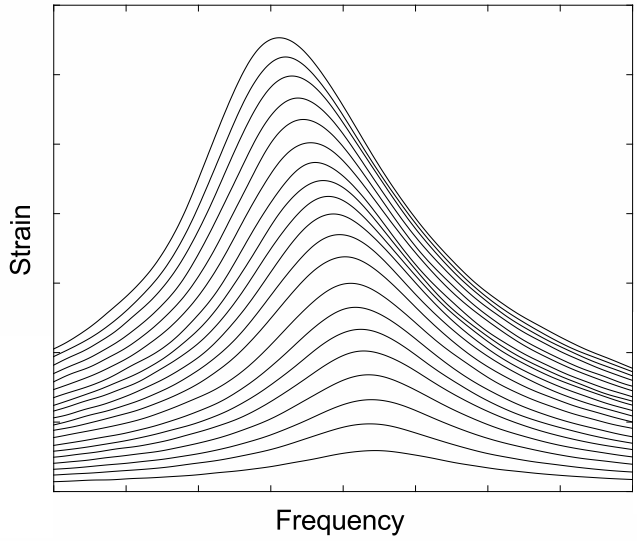

Figure 5: Typical resonance response of a nonclasscial material

Figure 5 gives a typical nonlinear strain over frequency response, where the negative frequency shift for increasing excitation shows softening material character. The frequency shift Δf over strain amplitude $\Delta\epsilon$ specifies the hysteretic nonlinearity parameter, α, with

$$\frac{\Delta f}{f_0} = \frac{f - f_0}{f_0} = \alpha \Delta \epsilon, \tag{3}$$

where f_0 is the equilibrium or base frequency. For these measurements all of the various resonance modes of a material sample can be utilized.

Previous research applied the NRUS technique to very different materials including rocks, composites, bone and metal, using various techniques for sample excitation such as piezo-electric transducers [25], impact hammers [3], electromagnetic transducers [24] or loudspeakers [29] [31]. For the detection of the sample motion there is also a variety of components commonly used, such as contact-based piezo-electric transducers and accelerometers or noncontact detection with laser vibrometers.

2.3 Vibrations of a Free Bar

This section describes the longitudinal vibrational behavior of thin bars, defining the strain, longitudinal wave equation and natural frequencies for free-free boundary condition as shown by Kinsler [17].

2.3.1 Longitudinal Strain

First, assume a longitudinal loaded, long and thin bar with constant cross-sectional area S over length L that experiences a displacement $u = u(x, t)$, persistent for each cross-section.

Within the bar a segment of width dx beginning at x and ending at $x + dx$ is defined (Figure 6). Through the application of the force the left segment boundary plane moves by u to the right and the left boundary plane moves $u + du$ to the right. For very small strains the first two terms of the Taylor's series expansion for u over

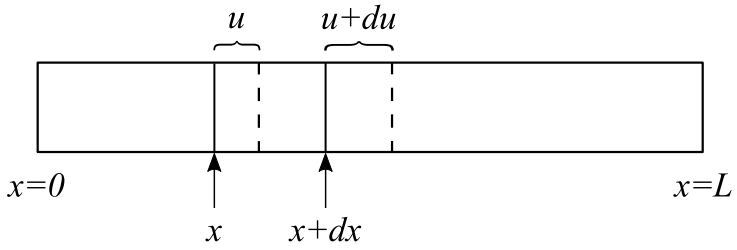

Figure 6: Longitudinal strain in a bar [17, Fig. 3.1]

x can be stated as

$$u + du = u + \left(\frac{\partial u}{\partial x}\right) dx \tag{4}$$

and the increase in length compared to its original bar length is then given by

$$(u + du) - u = du = \left(\frac{\partial u}{\partial x}\right) dx. \tag{5}$$

Hence, for the strain ϵ, the ratio between increase in length to original length, follows

$$\epsilon = \frac{\left(\frac{\partial u}{\partial x}\right) dx}{x} = \frac{\partial u}{\partial x}, \tag{6}$$

a function of x and also t.

2.3.2 Longitudinal Wave Equation

Figure 7: Compressional forces on a bar segment [17, Fig. 3.2]

On each cross-sectional plane in a strained bar act longitudinal forces $F = F(x, t)$ that induce stress $\sigma = F/S$. For small strains Hooke's law applies that states a proportional relationship between stress and strain,

$$\sigma = -E\frac{\partial u}{\partial x}, \tag{7}$$

where E is the Young's modulus. This leads rewritten for the internal longitudinal forces F to

$$F = -SE\frac{\partial u}{\partial x}. \tag{8}$$

The internal force at x is F and at $x + dx$ acts $F + (\partial f/\partial x)$. This leads to a net force to the right of

$$dF = -F - \left(F + \frac{\partial F}{\partial x}dx\right) = -\frac{\partial F}{\partial x}dx. \tag{9}$$

Substitution of (8) leads then to

$$dF = SE\frac{\partial^2 u}{\partial x^2}dx. \tag{10}$$

Including the mass property, the mass of the segment dx becomes $\rho S dx$ with the density ρ leading to the equation of motion of the segment

$$(\rho S dx)\,\frac{\partial^2 u}{\partial t^2} = SE\frac{\partial^2 u}{\partial x^2}dx. \tag{11}$$

With $c^2 = E/\rho$, where c is the phase velocity this finally yields to the longitudinal wave equation of the displacement field

$$\frac{1}{c^2}\frac{\partial^2 u}{\partial t^2} = \frac{\partial^2 u}{\partial x^2}. \tag{12}$$

The complex harmonic solution of the longitudinal wave equation (12) is given by

$$\boldsymbol{u} = \boldsymbol{A}e^{i(\omega t - kx)} + \boldsymbol{B}e^{i(\omega t + kx)} \qquad \text{with} \qquad k = \frac{\omega}{c}, \tag{13}$$

where $\boldsymbol{A}$ and $\boldsymbol{B}$ are amplitude constants and k is the wave number.

2.3.3 Resonant Bar in Free-Free Boundary Condition

Let's assume a bar in completely free space with no boundary condition attached. For this state, called free-free boundary condition, the strain at $x = 0$ and $x = L$ becomes zero. $\partial \boldsymbol{u}/\partial x = 0$ at $x = 0$ leads to

$$-\boldsymbol{A} + \boldsymbol{B} = 0 \Longleftrightarrow \boldsymbol{A} = \boldsymbol{B}, \tag{14}$$

so that (13) reduces to

$$\boldsymbol{u} = \boldsymbol{A}e^{i\omega t}\left(e^{-ikx} + e^{ikx}\right) = 2\boldsymbol{A}e^{i\omega t}cos\,(kx)\,. \tag{15}$$

Plugging in $\partial \boldsymbol{u}/\partial x = 0$ for $x = L$ into (15) gives $sin\,(kL) = 0$ leading to the natural frequencies

$$\omega_n = \frac{n\pi c}{L} \quad \text{or} \quad f_n = \frac{n}{2}\frac{c}{L} \quad \text{with} \quad n = 1, 2, 3, ... \tag{16}$$

and the eigenmodes are described by

$$\boldsymbol{u_n} = 2\boldsymbol{A_n} e^{i\omega_n t} cos\,(k_n x) \quad \text{with} \quad k_n = \frac{\omega_n}{c} \quad \text{and} \quad n = 1, 2, 3, ... \tag{17}$$

with the longitudinal displacement patterns depicted in Figure 8.

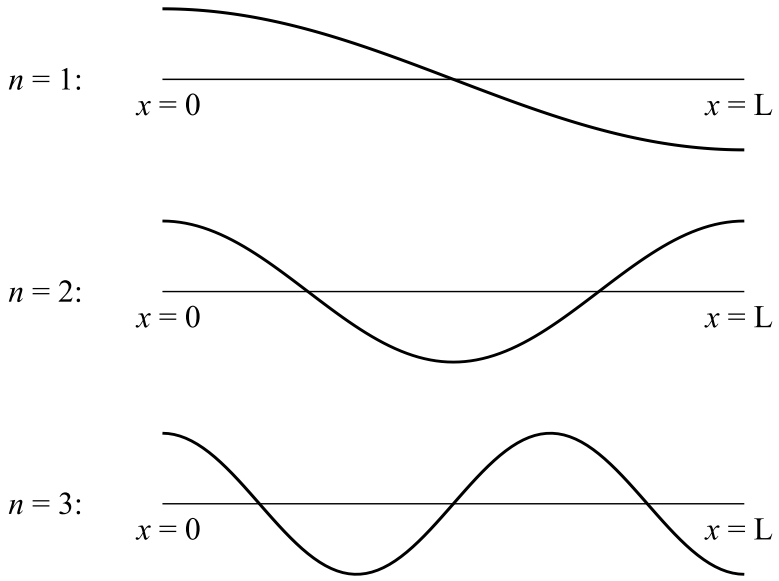

Figure 8: Standing longitudinal wave patterns of the first three longitudinal eigenmodes of a bar in free-free boundary condition [17, Fig. 3.3]

CHAPTER III

MATERIAL

To evaluate the capabilities of the NRUS experimental setups materials with different nonlinear behavior are tested. Aluminium and stainless steel, for which other research [13] identified a large difference in the hysteretic nonlinearity parameter, α, are used to validate the measurement techniques. To investigate the sensitivity to microscopic material damage in metallic materials, a series of thermally aged 17-4PH stainless steel is used. This steel was chosen because a series of heat treatments is already executed and experimental results such as Vickers hardness, thermo-electric power and β-measurements are also already available for these samples.

The following sections introduce the used 17-4PH stainless steel and describe briefly its material properties and precipitation hardening processes, the applied heat treatment and the resultant material conditions.

3.1 Properties of 17-4PH Stainless Steel

17-4PH stainless steel is a very commonly used martensitic precipitation-hardening ("PH") alloy with a good combination of high-strength, good ductility and corrosion resistance. The steel contains about 3 wt. % Cu and is strengthened by precipitation of dispersed copper particles in the martensite matrix [22].

Solution annealed 17-4PH shows initially no copper precipitates. Thermally aging at temperatures of 400°C and higher hardens the material [21]. At first, coherent copper-rich precipitates form increasingly in the material, restraining dislocations in the matrix. The copper has a low solubility at this temperature such that the copper atoms diffuse and form fine particles. After exceeding peak aging time the growing copper-rich precipitates become incoherent with the matrix, which now leads to lower

strength and hardness. [14]

Previous research [8] [18] concentrated their work on 17-4PH stainless steel because of similarities of the microstructure to irradiated reactor pressure vessel (RPV) steel. Radiation damage leading to embrittlement is also partly caused by copper-rich precipitates of similar size and density and they used 17-4PH as a surrogate to avoid difficulties in handling irradiated steel samples.

3.2 Material Preparation

The chemical composition of the 17-4PH stainless steel as-received is given in Table 1. The steel has a tensile strength of 1384 $\mathrm{N/mm^2}$ and a yield strength of 1263 $\mathrm{N/mm^2}$ and is solution annealed at 1040°C for 6 h followed by air cooling.

Table 2 gives an overview of the applied thermal aging processes. The designation reference geometry refers to the original shape for previous experiments before cut to the desired sample dimensions for this research. All but one of the bar samples were thermally aged as-received at 400°C for 0.1 to 6 h. The same was done on some samples from the Charpy reference geometry, skipping the 0.1 h aging time step. A second batch was again solution annealed at a higher temperature of 1100°C, but then gas quenched with high pressure gas before thermally aged. The second annealing step with higher cooling rate has the purpose to prevent precipitation formation during cooling time.

Table 1: Chemical composition of received 17-4PH stainless steel

C	Cr	Cu	Ni	Mn	Si	Nb
0.023	15.15	3.07	4.46	0.63	0.46	0.26
Mo	Co	N	P	S	Ti	Fe
0.08	0.044	0.02	0.016	0.001	0.001	rest

Table 2: Sample designations and heat treatment procedure for 17-4PH samples

Reference geometry	Sample designation	Solution annealing	Cooling method	Aging time @ 400°C
bar	AC	1040°C/6 h	air cooled	-
	AC-0.1	1040°C/6 h	air cooled	0.1 h
	AC-1	1040°C/6 h	air cooled	1 h
	AC-6	1040°C/6 h	air cooled	6 h
Charpy	AC	1040°C/6 h	air cooled	-
	AC-1	1040°C/6 h	air cooled	1 h
	AC-6	1040°C/6 h	air cooled	6 h
	GQ	1100°C/2 h	gas quenched	-
	GQ-1	1100°C/2 h	gas quenched	1 h
	GQ-6	1100°C/2 h	gas quenched	6 h

3.3 Material Condition

The following tests are already performed by Thiele [28] and Matlack [18]. These measurements allow us to compare the hysteretic nonlinearity parameter to the hardness, the thermo-electric power and the acoustic nonlinearity parameter.

3.3.1 Vickers Hardness Measurements

The Vickers hardness measurements were performed with a Buehler High Quality Hardness Tester for multiple measurement locations in lateral and transversal directions to include potential anisotropic material characteristics.

The results, shown in Figure 9, indicate a clear increase in hardness over aging time for the samples with Charpy and bar reference geometry in a manner consistent with the work of Mirzadeh and Najafizadeh [21]. The hardness level for the gas quenched samples is as expected about 60 HV lower than for the air cooled samples due to the suppression of initial precipitation forming after the solution annealing

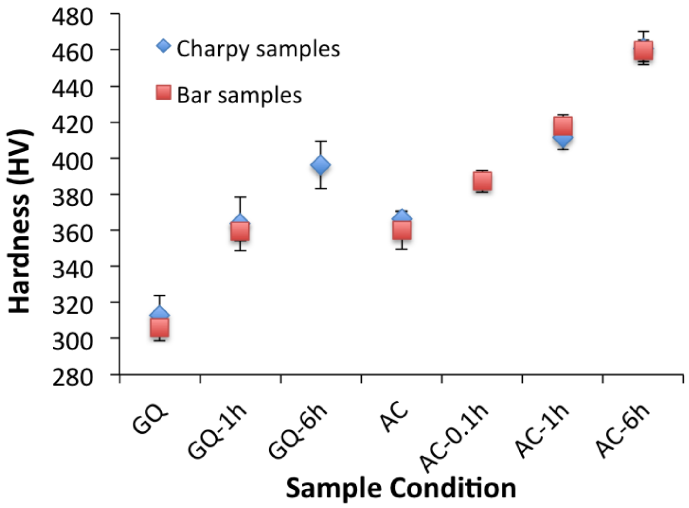

Figure 9: Vickers hardness for thermally aged 17-4PH Charpy and bar samples [18, Fig. 24]

through a faster cooling rate.

3.3.2 Thermo-electric Power Measurements

For the thermo-electric power (TEP) measurement technique the voltage difference, generated by a temperature gradient in the material sample, is measured and compared to a reference material. The measurements are quantified by the Seebeck coefficient $S = \Delta V/\Delta T$, the ratio between voltage difference and temperature gradient [23]. TEP measurements have shown to be strongly sensitive to microstructural evolution such as precipitation formation. Rana et al. [26] have shown that the Seebeck coefficient increases due to coherency strains and decreases due to dislocations.

Multiple measurements at different locations are performed with a Koslov Thermo Electric Alloy Sorter TE-3000, calibrated with a Hastelloy C-27 steel probe, and are depicted in Figure 10. The values show for all materials a steady increase for progressive thermal aging.

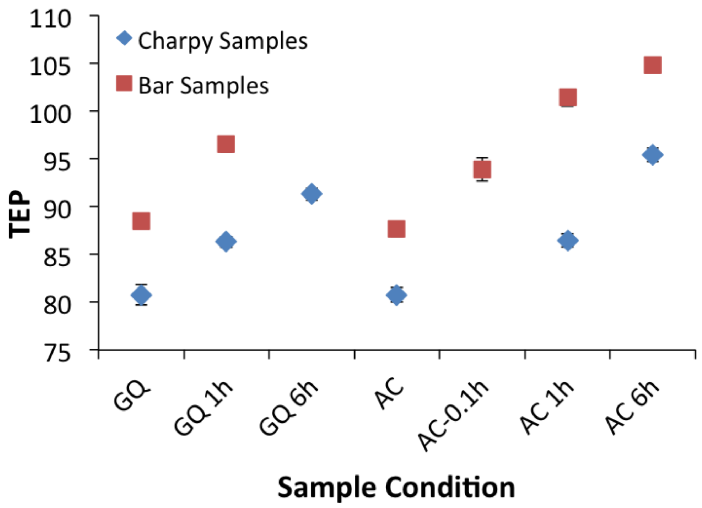

Figure 10: Thermo-electric power for thermally aged 17-4PH Charpy and bar samples [18, Fig. 25]

3.3.3 β-Measurements

Figure 11 shows the normalized relative acoustic nonlinearity parameter, β', for the samples measured with a Rayleigh surface wave based technique. A piezoelectric transducer attached to a plexiglass wedge that is pressed down onto the specimen excites Rayleigh surface waves which are detected at various locations along the propagation path with an air-coupled piezoelectric transducer. The nonlinear material behavior is quantified by evaluating the ratio A_2/A_1^2 of the amplitudes of the first (A_1) and second harmonics (A_2) at different wave propagating distances. The slope of the generated curve is proportional to the acoustic nonlinearity parameter, giving a relative distinction between the samples.

For both, the gas quenched and air cooled bar samples, the nonlinearity parameter decreases with increasing thermal aging time relative to the nontreated condition.

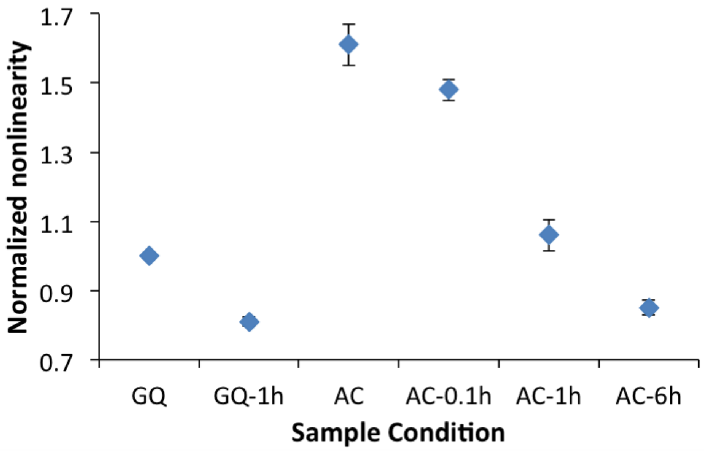

Figure 11: Normalized relative acoustic nonlinearity parameter, β', for thermally aged 17-4PH Charpy and bar samples using Rayleigh surface waves from Thiele et al. [28] [18, Fig. 30]

CHAPTER IV

NONLINEAR RESONANCE ULTRASOUND SPECTROSCOPY FOR SMALL PLATES USING CONTACT EXCITATION

The following chapter explains the experimental setup, included components and techniques and describes the signal processing steps to assess the nonlinearity of small rectangular plates. To validate the measured resonance frequencies, the eigenmode shapes and corresponding frequencies are simulated with the COMSOL Multiphysics Software and compared to the experimentally gathered data. Furthermore, the system nonlinearity will be discussed and influencing parameters will be described. Finally, the experiment will be performed for a series of 17-4PH stainless steel samples with different heat treatments and the results and their significance, the limitations of the setup and consequences of these will be evaluated.

The Labview code controlling the measurement protocol and data acquisition is taken over from Forstenhäusler [8] and his work on the data processing provides the basis for the data processing steps performed in this research.

4.1 Experimental Setup

The schematic of the experimental setup for the nonlinear resonance ultrasound spectroscopy (NRUS) measurements is displayed in Figure 12. It consists of a function generator connected to a longitudinal piezoelectric transducer with an amplifier in between. A small rectangular plate with dimensions of 10 mm x 10 mm x 2 mm is fixed between the transducer and a steel base at two opposite edges. The transducer

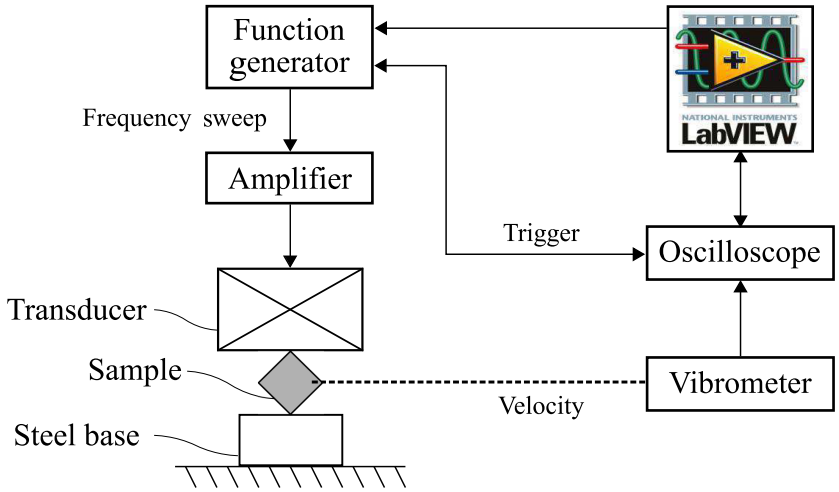

Figure 12: Schematic of experimental setup for NRUS measurements of small plates

excites the sample and a laser vibrometer detects the out-of-plane motion of the surface. An oscilloscope connected to the trigger of the function generator and to the vibrometer records the velocity and the trigger signal. The whole setup is controlled by a Labview code on a computer that also collects and stores the data.

As shown in Figure 13 the transducer is fixed to a linear guiding by an aluminium mounting plate. The linear guiding allows the transducer to move freely in the vertical direction and contains an internal helical spring that counterbalances the weight of the fixture including the transducer and attached weight holder. By bolting down the linear guiding on different heights onto a 90° angle bracket fixed to the lab bench, the initial pressure on the specimen can be varied and an extension arm pressing on a digital scale as shown in Figure 25 allows us to determine the exact initial weight on the specimen. By adding weights into the 3D-printed weight holder shell this force can be further increased.

To position the sample accurately and repeatedly to the exact same position the sample holder pictured in Figure 14 was developed. The sample holder is a vertically adjustable linear guiding attached to a 90° angle bracket. The sample itself is held by a magnetic strip onto a 3D-printed part bolted to the vertical slider and fixed

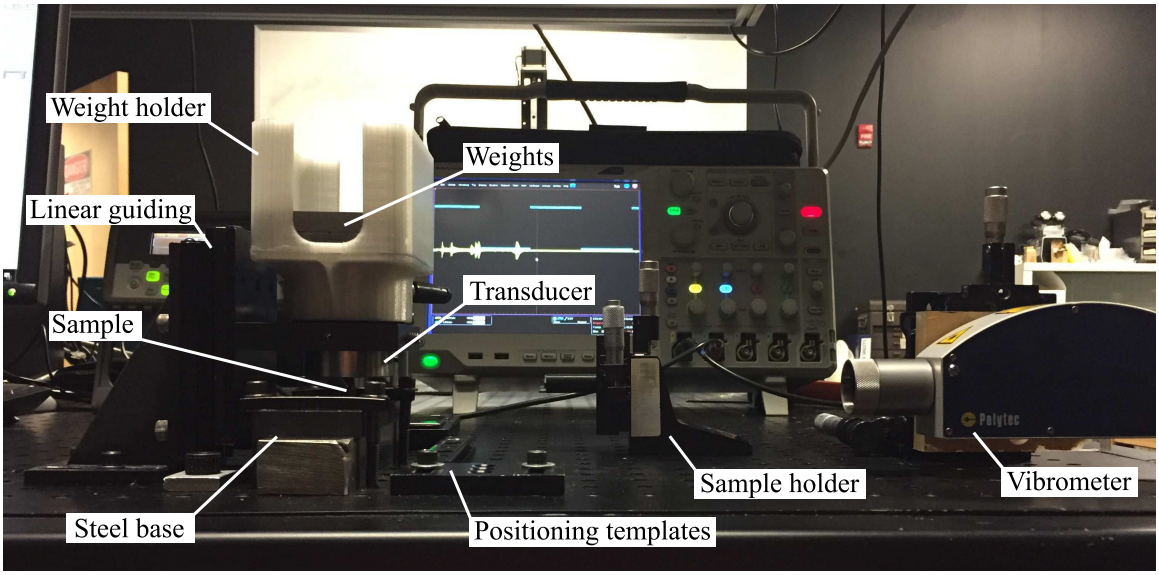

Figure 13: Picture of experimental setup for NRUS measurements of small plates

positioning templates on the main bench act as stops for the sample holder. For this measurement setup it is essential that the specimen is exactly vertical so that the edges are flush to the transducer's contact surface and the pressure is evenly distributed to get a maximal contact surface for high excitations. It is also necessary that the surface of the specimen is orthogonal to the laser beam and in a specified distance to the vibrometer, determined by the focal length.

4.1.1 Samples

The samples are EDM-cut (Electrical discharge machining) slices of previously heat treated and milled 10 mm x 10 mm steel Charpy bars, introduced in chapter 3. Because the laser detection requires a reflective surface one side on the plates is wet polished with very fine abrasive paper. It has shown that with the sharp edges from the machining the excitation of the specimen is not strong enough to achieve sufficient out-of-plane displacement. By rounding the edges slightly by hand with fine abrasive paper and therefore increased contact area the motion is significantly increased.

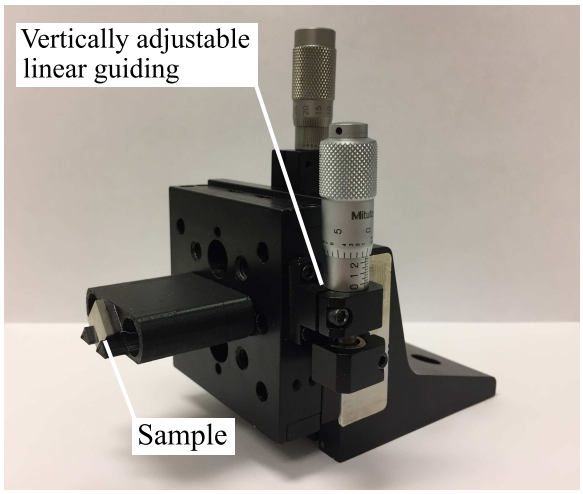

Figure 14: Picture of the sample holder, the device to hold and position the small plate samples in experimental setup

4.1.2 Function Generator with Power Amplifier

The function generator Agilent 33250A produces a continuous sinusoidal signal of specified frequency and amplitude. While the amplitude is held constant for each individual sweep the frequency increases constantly between set boundary values. The function generator is capable of generating a sinusoidal signal with a peak-to-peak voltage of 20 V. To increase specimen excitation further a 20 kHz - 10 MHz power amplifier ENI 240L is used to amplify the signal up to 80 V peak-to-peak. The trigger connection between function generator and oscilloscope enables determining the start and end point of each individual frequency sweep.

4.1.3 Transducers

For sufficient excitation of the sample with high displacement amplitudes a low frequency narrow band Panamterics 1.25 inch contact transducer X1021 with nominal frequency of 50 kHz is selected. Driven by the sinusoidal voltage it generates longitudinal waves and transmits them over the small contact patch into the specimen. In comparison with a very similar 50 mm Ultran transducer GRD50-D50 with equivalent nominal frequency but a softer contact surface, the Panamterics transducer with

harder wear face achieves higher out-of-plane excitations of the specimen.

For longer frequency sweeps up to 200 kHz to identify the eigenmodes a smaller 1 inch Panamterics 250 kHz transducer with higher nominal frequency is used. Not sweeping through the resonance frequency of the transducer itself helps comparing the displacement magnitudes of the eigenmodes relative to each other.

4.1.4 Laser Vibrometer

The Polytech 1-dimensional Laser Doppler Vibrometer (LDV) used in this study is capable of measuring the velocity of the sample surface up to minimal velocities of 0.1 μm/s in a wide frequency bandwidth. The advantage of a laser vibrometer over other techniques is to measure the out-of-plane displacement of the sample without disturbing its motion. Other types of sensors that are need to be attached to the sample add mass to the system and impair the movement of the specimen.

The Polytech OFV-5000 Vibrometer Controller also contains a build in low and high pass filter which are set to 1.5 MHz and 100 kHz to smooth the signal before being displayed and processed by the oscilloscope.

4.1.5 Setup Control and Data Collection

The function generator and the Tektronix 5034B oscilloscope are linked to a computer via a GPIP and an Ethernet connection respectively and are controlled by Labview. The Labview code specifies the excitation parameters via the function generator, controls the recording settings of the oscilloscope and stores the velocity signal as well as the trigger signal on the computer.

4.2 Measurement Procedure and Data Processing

To obtain the frequency domain response a window function is applied on each individual time domain signal (Figure 15a) and a fast Fourier transformation (FFT) is performed. The resulting frequency domain response depicted in Figure 15b shows

the velocity response over the excited frequencies. To determine the peak velocity and corresponding resonance frequency most precisely, the signal gets filtered by a zero-phase filter and a third order polynomial curve approximates a small range around the peak as shown in Figure 16.

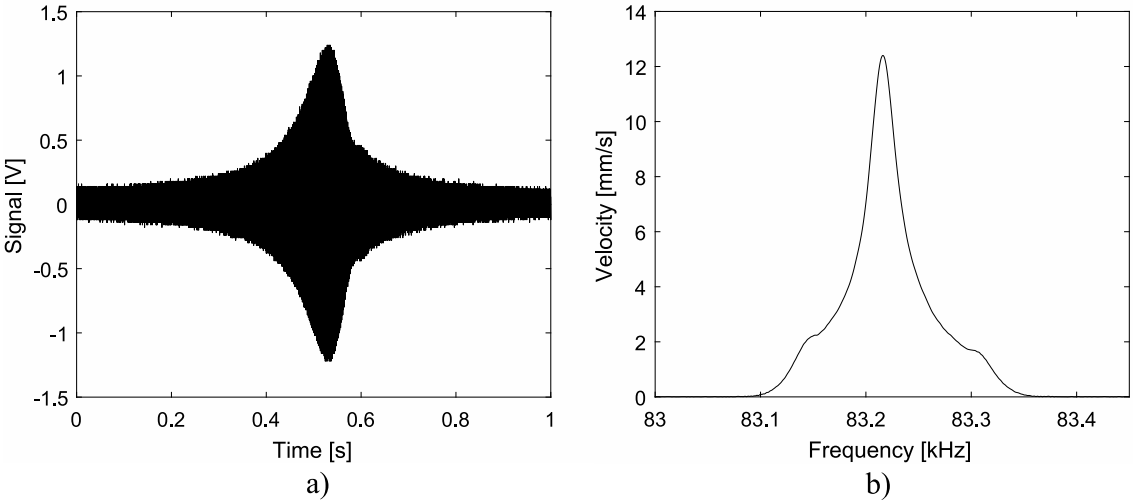

Figure 15: a) Time domain signal and b) frequency domain response

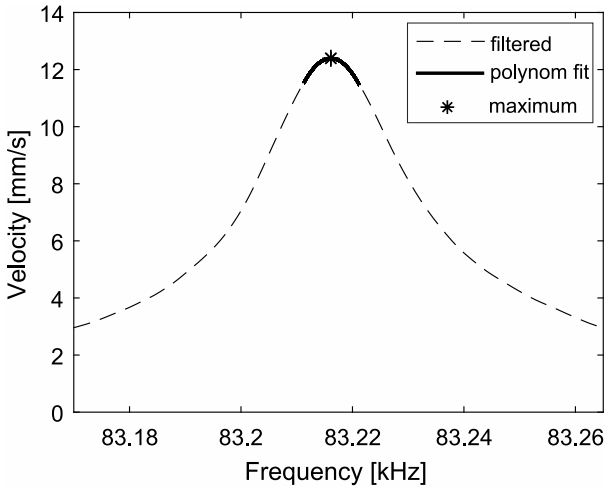

Figure 16: Peak fit and maximum of filtered frequency domain response

The chosen frequency bandwidth around the equilibrium resonance frequency is $f_0 \pm \Delta f$, where $\Delta f = 0.5\%$ with a sweep duration of 1 s at a sampling rate of 500 kSa/s. The process of determining and selecting an eigenmode and corresponding frequency f_0 is described in detail in section 4.3.3.

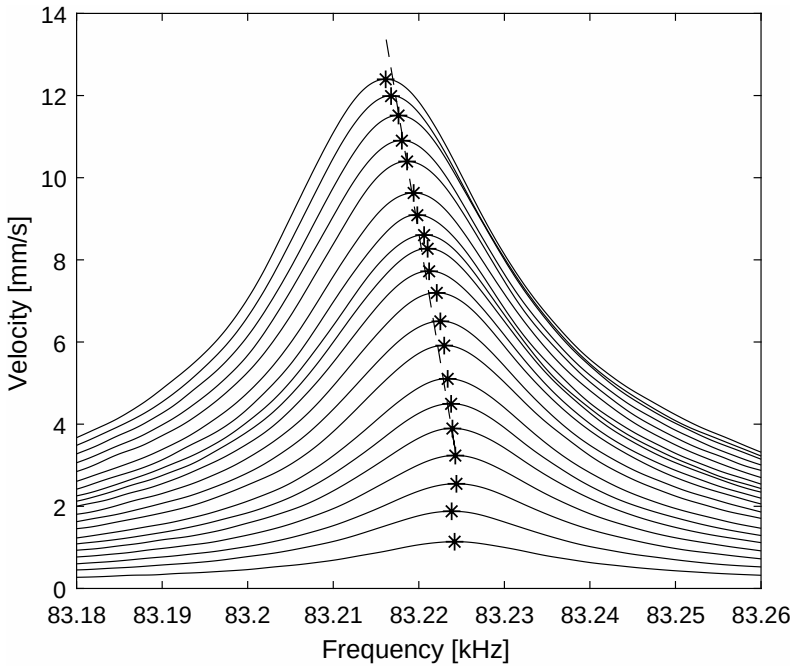

Figure 17: Frequency response for different driving amplitudes

By repeating this process for 20 equally spaced and increasing voltage steps, Figure 17 is generated that shows a decreasing resonance frequency for increasing voltage amplitudes. To visualize the frequency shift for normalized resonance frequencies Figure 18a is generated by dividing the frequency shift $\Delta f = f - f_0$ for each excitation level by the equilibrium frequency f_0, which is determined by intersecting the linear fit of Figure 17 with the x-axis.

As stated of the resonance frequency in chapter 2, the hysteretic nonlinearity parameter, α, is defined in dependence on the strain ϵ in the specimen and therefore a relationship between the measured velocity and strain in the specimen is needed to determine α. Due to the complex strain distribution it was not possible to develop such an analytical relationship and an absolute nonlinearity parameter for this measurements keeps indeterminate. Instead a relative nonlinearity parameter, α' that represents the slope of the linear fit and corresponds to $C\alpha$, where C is a constant, is defined. The volumetric strain distribution, solved with a FEM software, is given in section 4.4.

Since the individual data points and the linear fit apparently do not fit well, a methodology adopted from Haupert et al. [13] that compensates temperature changes during the measurements, is included. This extended procedure includes measuring the resonance frequency in between each increasing driving step at a base voltage amplitude that is chosen to be, in this case, the lowest excitation level with narrowest resonance response. This means starting with the lowest level, then increasing the voltage level by one step, followed by measuring the lowest level again, then increasing the voltage level by two steps, lowering to the lowest level again and so on. If the experimental setup and sample do not experience any changes like temperature deviation during the whole measurement procedure these base level measurements should lead to the same resonance frequency. As shown in Figure 18b this is not the case for the present experimental environment. For this example of a measurement series the base resonance frequency first increases and for higher repetition steps decreases again. By subtracting the relative frequency shift of the base level excitation from the corresponding relative frequency shift of the increasing driving steps the corrected relative frequency shift of Figure 19 can be determined.

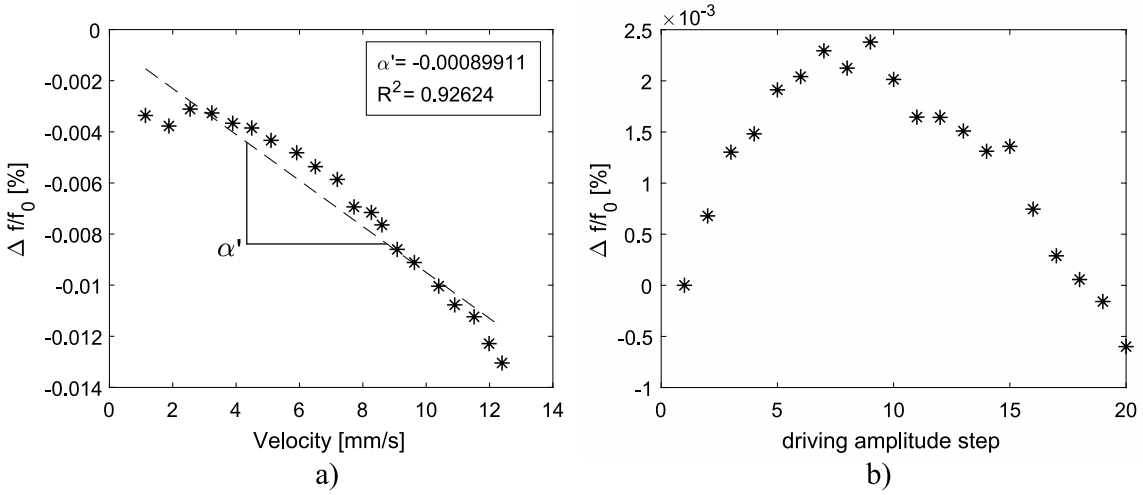

Figure 18: a) Relative frequency shift for different driving amplitudes and b) relative frequency shift of reference amplitude

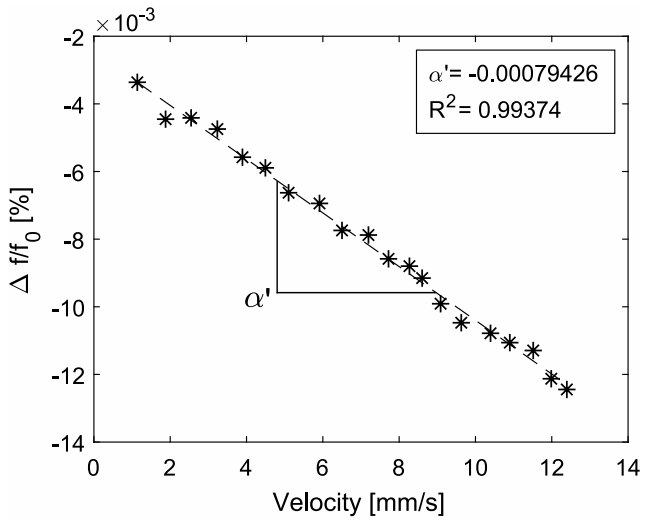

Figure 19: Corrected relative frequency shift for different driving amplitudes

The linear fit of the corrected relative frequency shift to the peak velocity over normalized frequency data points is now substantially improved. The average R^2-value of ten measurements increases from 0.941 ± 4.81 % without correction to an average R^2-value of 0.993 ± 0.534 % with included correction.

4.3 Modal Analysis

In order to understand the elastic distortion behavior of the specimen for different excitation frequencies, the sample is simulated with the finite element analysis software COMSOL Multiphysics 5.2. The simulation also provides an interpretation of the frequency spectrum for long sweeps as shown in Figure 21. Both, the experimentally determined frequency spectrum and the simulated visualization of the eigenmodes shapes, finally lead to the selection of significant eigenmodes.

4.3.1 Identification with FEM

Since the specimen is held by friction contact to both, the steel base and the transducer, the eigenmode shapes and corresponding natural frequencies are different to those of the specimen in a free boundary configuration. To match the experimentally

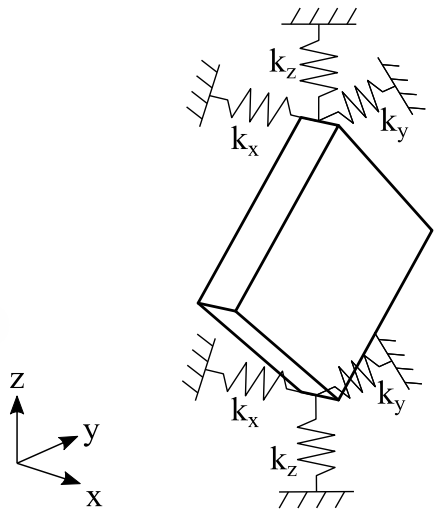

Figure 20: Visualization of the modulation of the contact conditions of the edges of small plate samples to the transducer and steel base surfaces by springs

gathered frequency spectra of Figure 21 with the natural frequencies of the simulation, the contact points are represented as *Spring Foundations*. This means that the edges of the specimen are not rigidly coupled to transducer and steel base, but elastic, assigned with a spring constant for each coordinate axis as schematically depicted in Figure 20. Currently it is not possible to modulate these contact interfaces as a *Contact Pair* with assigned friction coefficient in COMSOL Multiphysics 5.2, because the line contact of the edge on the flat surfaces of transducer and steel base don't have a therefore required resulting area.

By selecting isotropic values of $6.35 \times 10^9\,\mathrm{N/mm^2}$ as spring constants per unit length for all directions and both contact points, the first detectable eigenmode *mode 2* matches up by a difference of $0.008\,\%$ between simulation and experiment as Table 3 points out. The leading influential material property values of the density ρ, Young's modulus E and Poisson's ratio ν are kept to the COMSOL Multiphysics' default values of $7850\,\mathrm{kg/m^3}$, $210\,\mathrm{MPa}$ and 0.33 for steel, respectively.

Without implementation of further influential factors and effects the COMSOL eigenfrequency study leads to the displacement fields of the first eigenmodes and corresponding natural frequencies up to $150\,\mathrm{kHz}$ illustrated in Figure 21.

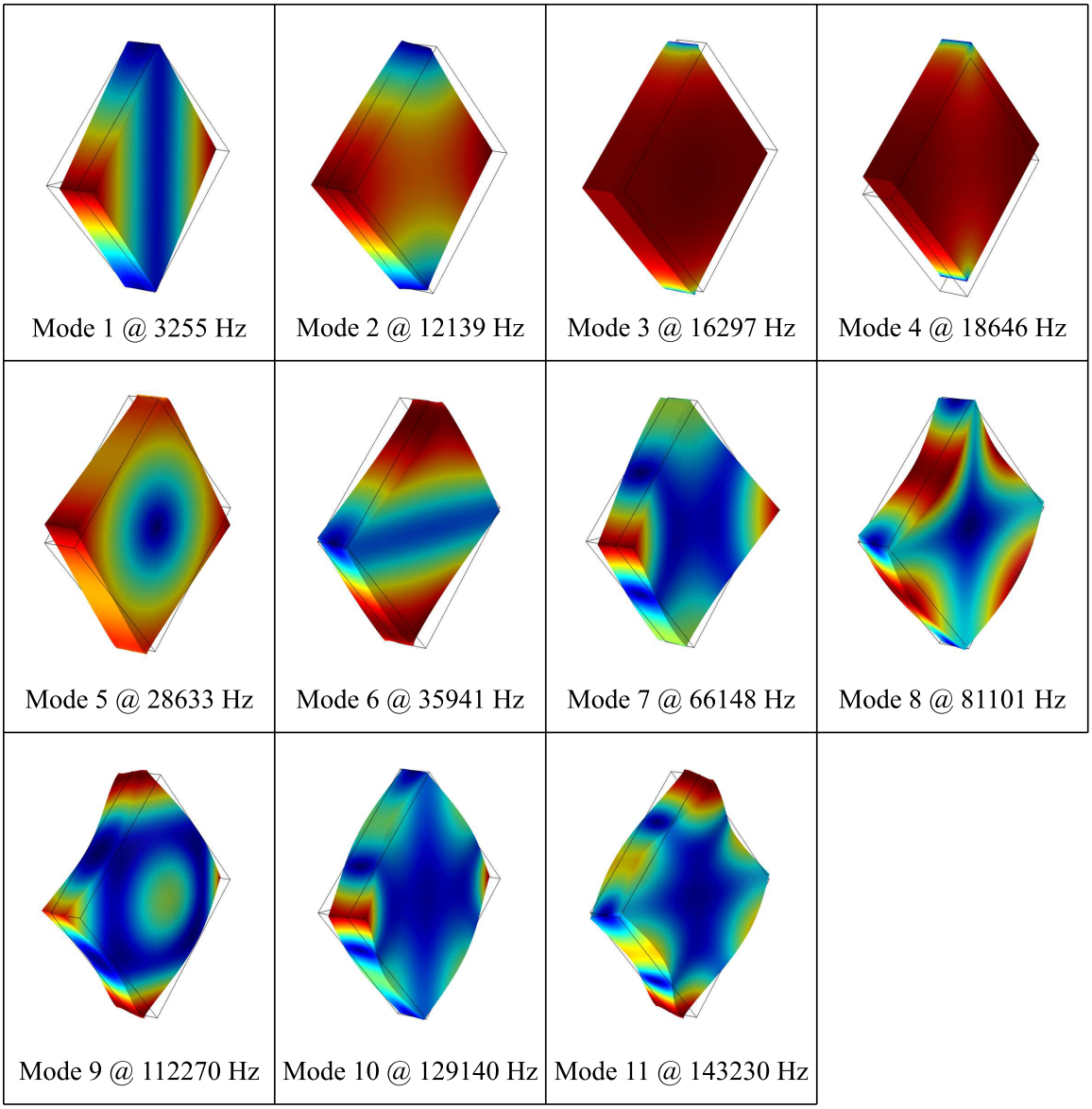

Figure 21: Displacement fields of the first eleven eigenmodes and corresponding natural frequencies of a stainless steel plate sample fixed between transducer and steel base up to 150 kHz. Arbitrary scaling of displacement amplitude with dark blue indicating no displacement and dark red colored surfaces indicating large displacement

4.3.2 Comparison to Experiment

The experimentally determined natural frequencies through long frequency sweeps are shown in Figure 22. The numbers associated with each resonance peak represent the corresponding eigenmode numbers introduced in Figure 21. By comparing the presence and height of a resonance peak for different survey points of the vibrometer with the eigenmode shapes from Figure 21, indicated by the small graphical depiction on the right, all eigenmodes besides *mode 1* and *mode 4-6* can be validated.

For example *mode 6* has no displacement on a horizontal line through the center of the plate. Therefore, the velocity of the surface and thereby a resonance peak can only be observed for a point not on this standing node line. This corresponds with the experimental frequency spectra, since the filtered frequency response for the points in the middle and near the corner show no peak, but the graph in the middle for a point over the center line does.

The first eigenmode shape *mode 1* persists in no deformation of the plate itself, but a rotation of the sample around its vertical axis. The decisive parameter for this behavior is probably the rotational stiffness of the contact conditions and since already mentioned in section 4.3.1 the simulation includes no specifically assigned parameter for that behavior. But since this eigenmode does not include deformation of the specimen, it is not of interest for this study anyway. The eigenmodes *mode 3*, *mode 4* and *mode 5* are not detectable, because their deformation does not include an out-of-plane component observable by the vibrometer.

The relatively small measured natural frequency denoted with a question mark at about 22 kHz is not explicable by the simulation. It is apparent that the peak height of this resonance increases with distance of the measurement point from contact point to steel base. This indicates that this is most likely a horizontal resonance behavior of the 90° angle bracket fixed to the lab bench including the linear guiding with aluminium mounting plate.

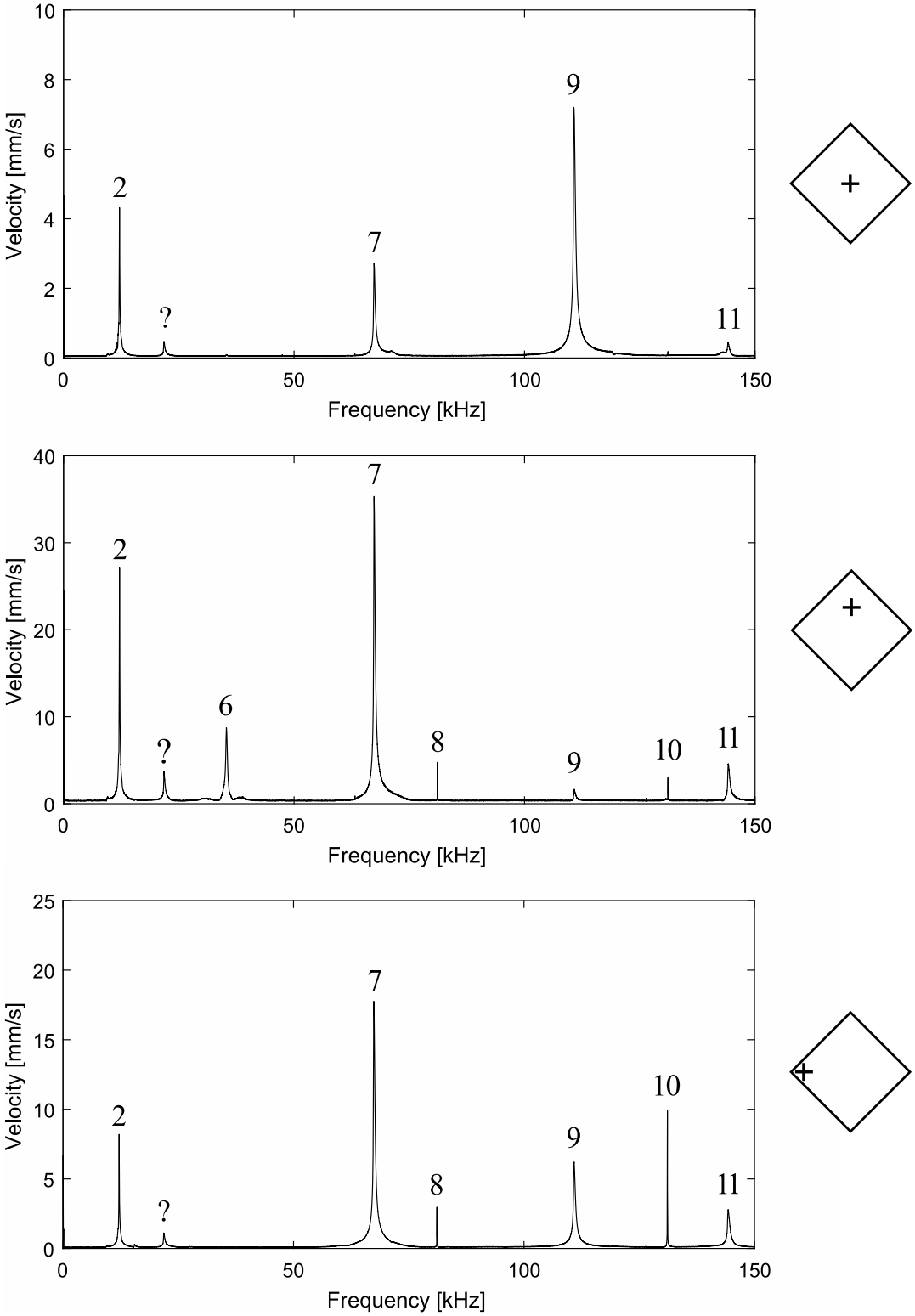

Figure 22: Filtered frequency response of the velocity for measurement points in the middle, between the middle and top corner and near left corner of the stainless steel plate sample and denotation of the corresponding eigenmodes

Table 3: Comparison of natural frequencies between experiment (f_{exp}) and simulation (f_{sim}) of a stainless steel plate sample

mode	f_{exp} [Hz]	f_{sim} [Hz]	$\lvert f_{sim} - f_{exp} \rvert$ [Hz]	$\frac{\lvert f_{sim} - f_{exp} \rvert}{f_{exp}}$	Q_{exp}
1	not detected	3255	-	-	-
2	12140	12139	1	0.008 %	159
3	not detectable	16297	-	-	-
4	not detectable	18646	-	-	-
5	not detectable	28633	-	-	-
6	35350	35941	591	1.672 %	117
7	67360	66148	1212	1.799 %	255
8	81110	81101	9	0.011 %	6240
9	110800	112270	1470	1.327 %	319
10	131100	129140	1960	1.495 %	8780
11	144200	143230	970	0.673 %	375

The maximal percental difference of simulated to experimental determined resonance frequency value is smaller than 1.8 % as Table 3 indicates.

4.3.3 Selection of Significant Eigenmodes

The eigenmodes *mode 8* and *mode 10* are eigenmodes that also exist for a plate sample in free boundary configuration with nearly identical displacement fields and only slightly reduced natural frequencies ($\Delta f < 0.5\%$). *Mode 8* and *mode 10* have also by far the highest quality factor Q, a dimensionless parameter quantifying the degree of damping and characterizing the "sharpness" of a resonance peak. The quality factor Q_{exp} for each eigenmode, calculated from the experimentally determined frequency spectrum by dividing their resonance frequency f_0 by their half-power bandwidth Δf_{hp} are given in Table 3. The lower the quality factor, the more damped the resonant behavior.

A explanation for this characteristic is provided by the movement of the edges of the sample in respect to the surfaces of transducer and steel base. This movement includes for all the detected eigenmodes despite *mode 8* and *mode 10* translation of the edges at the contact surfaces. The motion of the edges of *mode 8* and *mode 10* consist of pure rotation around the vertical axis. The dissipating energy absorbed by sliding friction describable by Coulomb damping is for the rotational case apparently much smaller.

To reduce the involvement of Coulomb damping in the measurements, the selection of significant eigenmodes is therefore narrowed down to *mode 8* and *mode 10*.

4.4 Volumetric Strain Distribution

As explained in section 4.2, it was not possible to develop an analytical velocity to strain relationship to determine the hysteretic nonlinearity parameter. Instead a relative nonlinearity parameter, α', was introduced. To compare the achieved strain level in the sample with other research, a time-dependent forced vibration simulation is used determine the average and maximum strain in the material.

To get the transient time-dependent solution for a forced vibration, a *Modal Time-Dependent Study* in COMSOL Multiphysics is performed. This modal-based analysis is a very efficient way to solve the time-dependent vibrational behavior of an object by reducing the dynamics of its structure to a combination of a small number of its most significant eigenmodes [4].

Figure 23 gives the transient solution of the velocity and the displacement of the forced vibration at 81 101 Hz for *mode 8*. The measuring point, indicated by the graphical depiction on the right, is close to an edge of the sample. For the picked modal time-dependent load the maximum velocity is 12.23 mm/s that approximately corresponds to the average maximum velocity achieved in the experiments. The maximum displacement of 2.33×10^{-5} mm/s is achieved at 7.75×10^{-5} s.

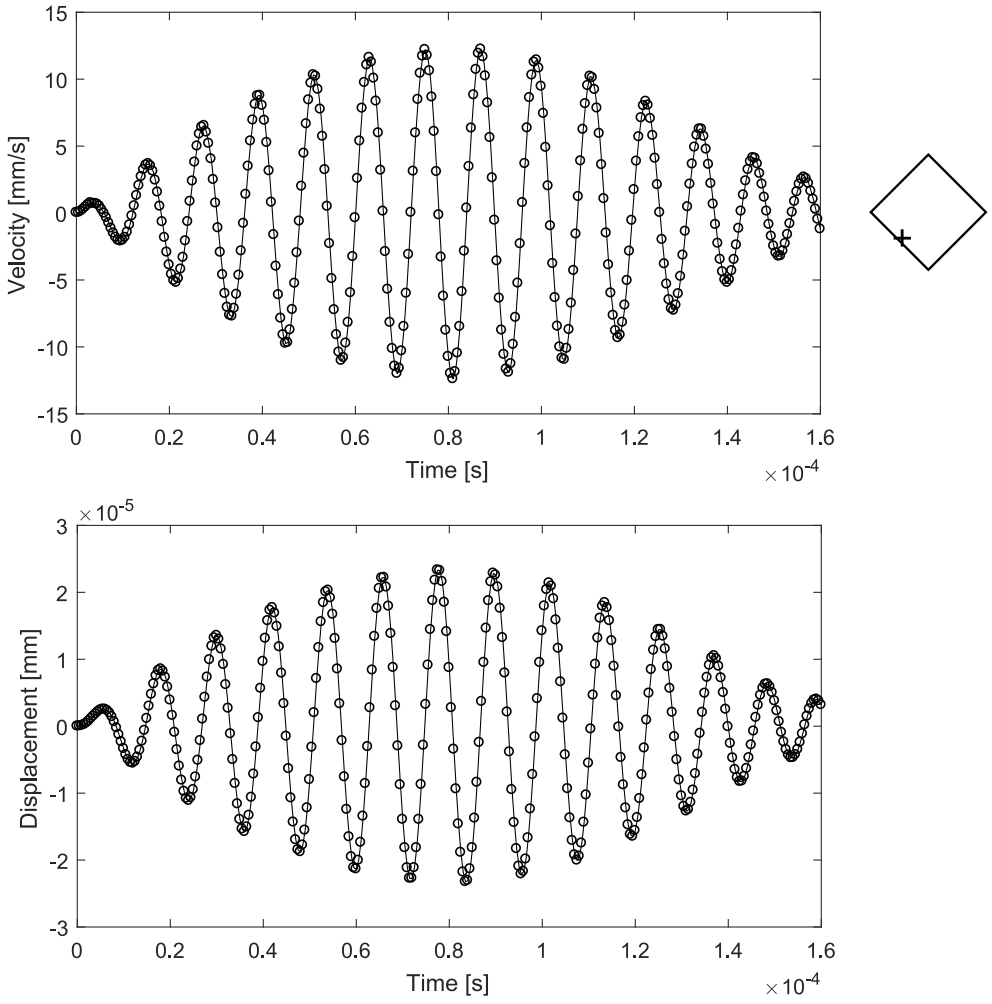

Figure 23: Transient time-dependent solution of velocity and displacement for a center point on an edge for forced vibration of *mode 8*, matched to the maximal excitation achieved with the experiment

The appendant Figure 24 gives the volumetric strain field for the time step with maximum displacement at 7.75×10^{-5} s. The maximum strain in the volume for this time step is 9.47e-7. This is very small compared to other NRUS research on metals [13] which achieved strain levels in stainless steel up to 3e-5.

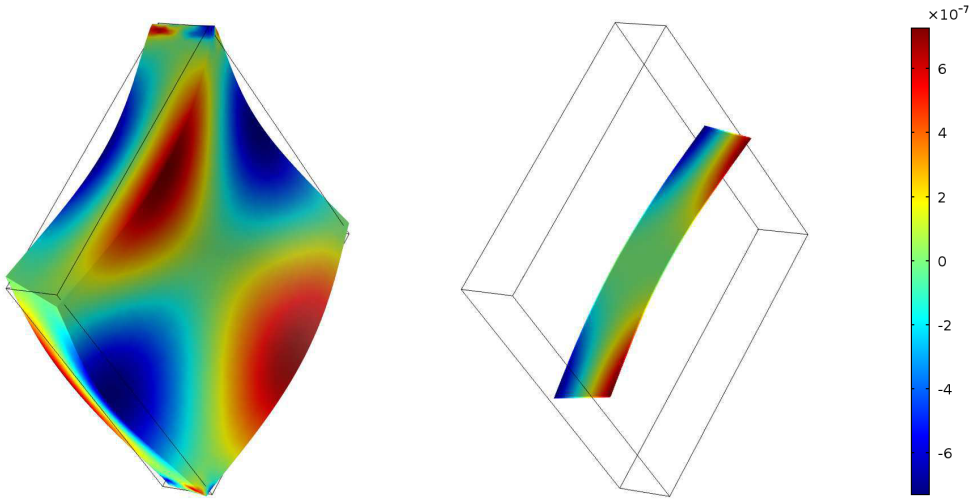

Figure 24: Volumetric strain contour of *mode 8* at 7.75×10^{-5} s on the surface (left) and in a center cross-section (right) of the stainless steel plate sample

4.5 System Nonlinearity

To determine accurately the material nonlinearity of the specimen, the nonlinear behavior of the involved experimental setup itself, including the electrical components, typically has to be negligibly small, especially when the material nonlinearity and its variation are expected to be quite small as in metallic specimens, considered in this work. Previous research [5] [28] identified transducers and amplifiers as sources of potential unwanted nonlinear influences to the measurements. Their approach to measure nonlinear material behavior, however, generated propagating longitudinal and Rayleigh surface waves, mainly dependent on the emitter parameters, not utilizing the resonance behavior of the specimen.

Because the concept of resonance ultrasound spectroscopy measurements exploits the natural amplification of the motion, the electrical components involved in the exciting of the specimen should not influence the measured nonlinearity. The measured quantities of interest the velocity amplitude and corresponding resonance frequency are like the whole motion of the specimen initiated, but not directly coupled to the

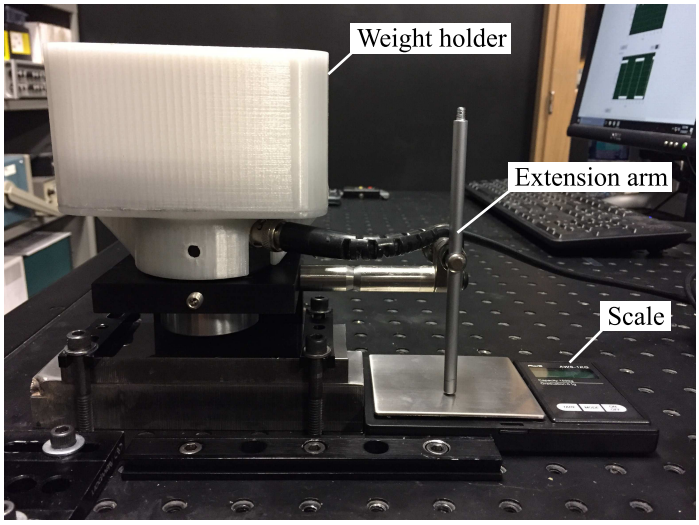

Figure 25: Picture of extension arm to experimental setup for NRUS measurements of small plates and scale

driving excitation and therefore do not include nonlinear effects of the excitation components.

4.5.1 Contact Pressure

The extension to the experimental setup shown in Figure 25 consisting of an extension arm and a scale allows measuring the exact weight and therefore equivalent force on the contact points of sample to transducer and steel base. By bolting down the linear guiding on different heights onto the 90° angle bracket the initial pressure or dead load on the specimen can be varied. The vertically adjustable extension arm pressing onto the scale maintains the correct height of the transducer when there is no sample fixed underneath the transducer. This is important because the helical spring inside the linear guiding is counteracting an upward directing force that is dependent on the vertical position of the transducer. By adding weights into the 3D-printed weight holder shell this force can be further increased.

Figure 26 and Table 4 show the relative nonlinearity parameter for the same measurement series of the same sample with increasing contact pressure by adding weights up to 4000 g to the initial force of equivalent 50 g. Two effects can be identified. First,

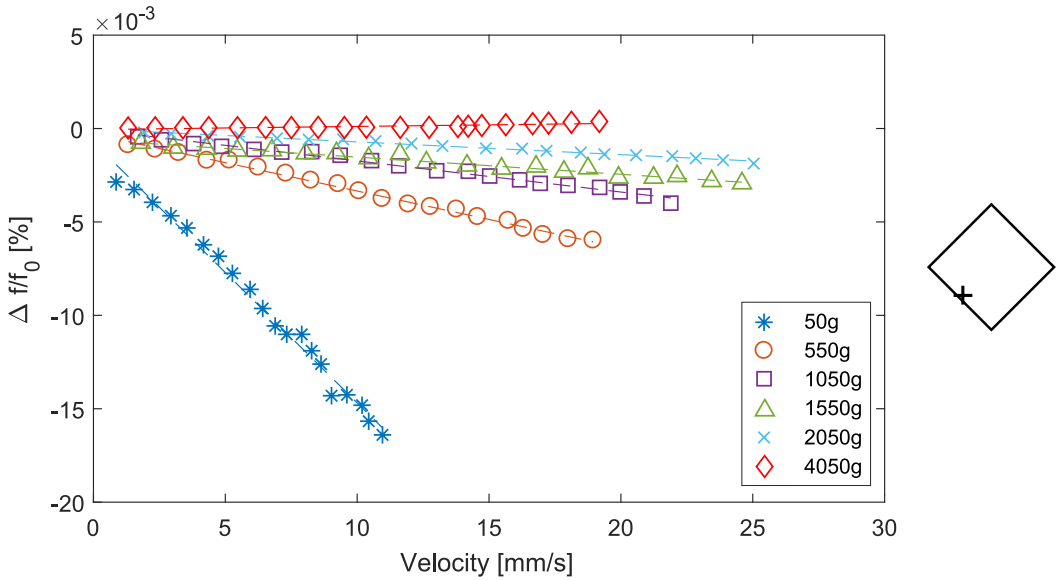

Figure 26: Nonlinear behavior of a stainless steel plate sample for increasing contact force by adding weights to the experimental setup

the increase in contact force leads to greater excitation and therefore higher peak velocities of the specimen. This effect is easy to comprehend, since the increased contact pressure leads to better energy transmission of the driving excitation in the contact point into the specimen.

Table 4: Comparison of f_0, v_{max}, α' and R^2 for NRUS measurements shown in Figure 26

added weight [g]	f_0 [Hz]	v_{max} [mm/s]	α'	$\Delta\alpha'/\alpha'_{50g}$	R^2
50	82915	10.96	-0.001395	0 %	0.9892
550	83103	18.96	-0.000304	-78 %	0.9945
1050	83152	21.89	-0.000167	-88 %	0.9884
1550	83179	24.59	-0.000110	-92 %	0.9660
2050	83194	21.89	-6.83e-05	-95 %	0.9725
4050	83220	19.21	1.67e-05	-101 %	0.8801

Second, the contact force has a very significant influence on the relative nonlinearity parameter, represented by the inclination of the slope. For the maximum force of 4000 g the determined linear fit indicates even a positive value for the frequency shift. This concludes to the assumption that the contact condition, which includes friction as stated in section 4.3.1 and further discussed in section 4.3.3, behaves nonlinear. This also leads to major uncertainties regarding the actual material nonlinearity of the specimen, since it is unclear whether the nonlinear contact behavior has an increasing or decreasing effect on the measured relative nonlinearity parameter, nor the extent of the proportion of this effect for each of the measurements.

4.5.2 Dependence on Selection of Eigenmode

NRUS measurements for eigenmodes with translational movement of the edge at the contact points such as *modes 2, 5-7, 9* and *11* result in implausible high frequency shifts. For instance, measurements with no additional weights for *mode 2* yield to α'-values of approximately -1e-2 which is about five times higher than for *mode 8* with the same measurement conditions. On the one hand this further affirms *mode 8* as the right choice as most significant eigenmode to determine the actual material nonlinearity of the specimen, but it also demonstrates again the influence of friction as a contributor to the measured nonlinearity.

4.6 Results for Thermally Aged 17-4PH Stainless Steel

Below, the RUS and NRUS results for the heat treated 17-4PH stainless steel samples from the Charpy reference geometry are shown. Each sample is measured five times by removing and placing it back again in the fixture on exactly the same edges in between each measurement.

The linear RUS results of the equilibrium frequency f_0 in Figure 27 show generally higher values for longer thermally aging, but the much larger increase in resonance frequency for the air-cooled samples and absence of change between AC-1 and AC-6

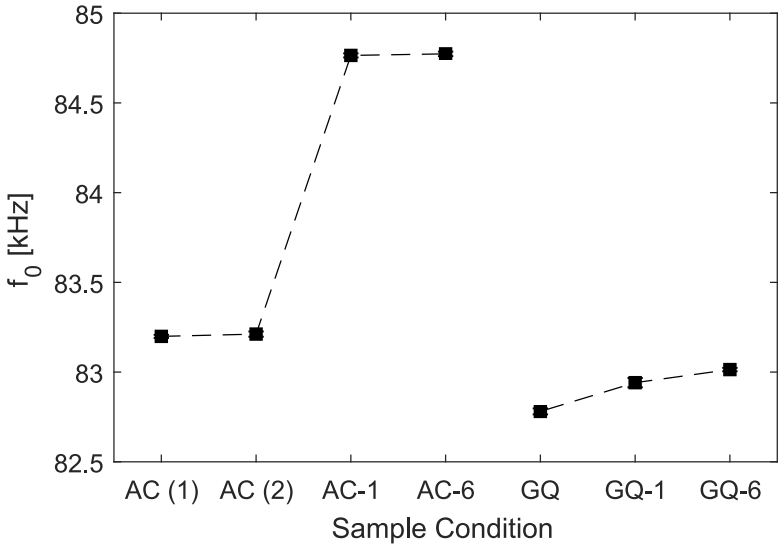

Figure 27: Results of RUS measurements for stainless steel plate samples with variations of heat treatments

challenges the validity of the results. Especially the fact, that the edges of the sample that are in contact to transducer and steel base are rounded by hand to increase sample excitation, which has influence on the resonance frequency, potentially affects the results significantly.

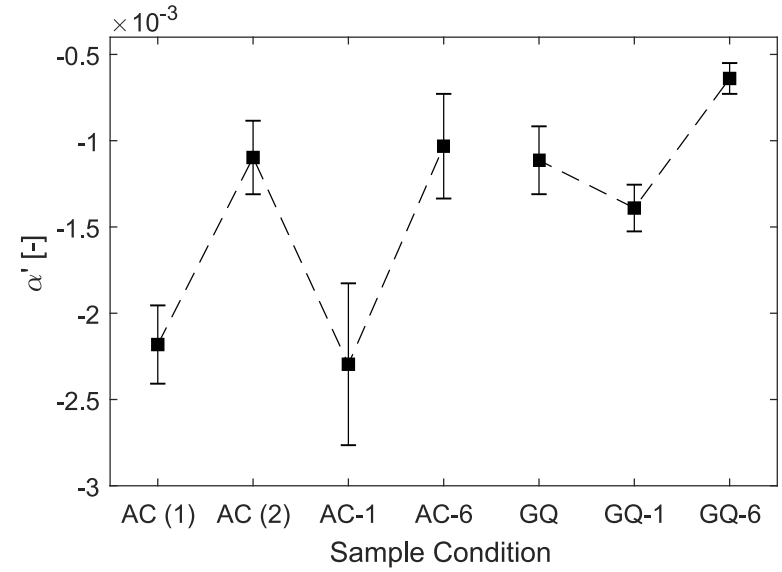

Figure 28: Results of NRUS measurements for stainless steel plate samples with variations of heat treatments

The NRUS results in Figure 28 show an average standard deviation of 17.28 %, indicating that the measurement values are repeatable for each specimen in a very limited order, but α' does not exhibit any favorable trend that can be expected base on physics. The NRUS measurements for the two AC samples with no heat treatment show a variation in mean value that spans almost the entire range of all measured α'-values, which demonstrates again that these values are not distinct and meaningful enough for statements about their material properties.

CHAPTER V

NONLINEAR RESONANCE ULTRASOUND SPECTROSCOPY FOR RODS AND BARS USING NONCONTACT AIR-COUPLED EXCITATION

Based on the results and experiences of the NRUS measurements for small plates in the previous chapter a conceptual varied setup is developed. Since chapter 4 clearly identified the contact points as a source of unwanted influence leading to no exploitable results, this new setup avoids contact to the excitation source by air-coupling the emitter.

This chapter introduces the modified experimental setup and explains the changes to the measurement protocol and data analysis procedure. Similar to the previous experiments the eigenmode shapes and natural frequencies are simulated and validated with COMSOL Multiphysics. Then, the measurements are performed for a series of heat treated 17-4PH stainless steel samples and the results and their significance are discussed.

5.1 Experimental Setup

In the modified experimental setup, depicted in Figure 29 and 30, the slender rod and bar samples are hanging horizontally in two wire straps. This fixation is intended to represent a free-free boundary condition, effective at least for longitudinal deformation and very small amplitudes. The laser vibrometer detects the longitudinal out-of-plane velocity at the flat surface at one end while a low frequency narrow band air-coupled transducer, extended with a focusing horn, excites the samples at the other end. The piezo-electric transducer with attached focusing horn is fixed onto a horizontally

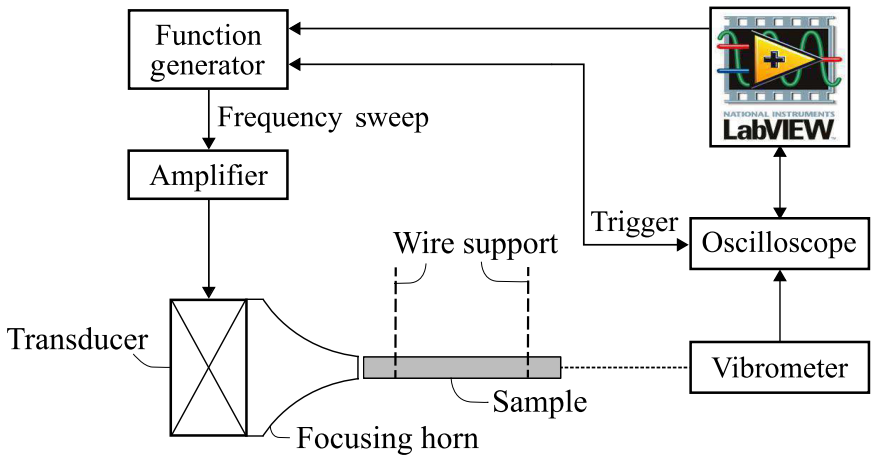

Figure 29: Schematic of experimental setup for air-coupled NRUS measurements of rods and bars

adjustable linear stage to vary the distance between horn throat and specimen.

The electrical components and data collection procedure is similar to the NRUS measurements for small plates in chapter 4. Labview controls the function generator and oscilloscope that are linked by a trigger connection and connected to the power amplifier and the vibrometer, respectively. Also Labview stores the gathered time domain signal and trigger signal data gathered by the oscilloscope.

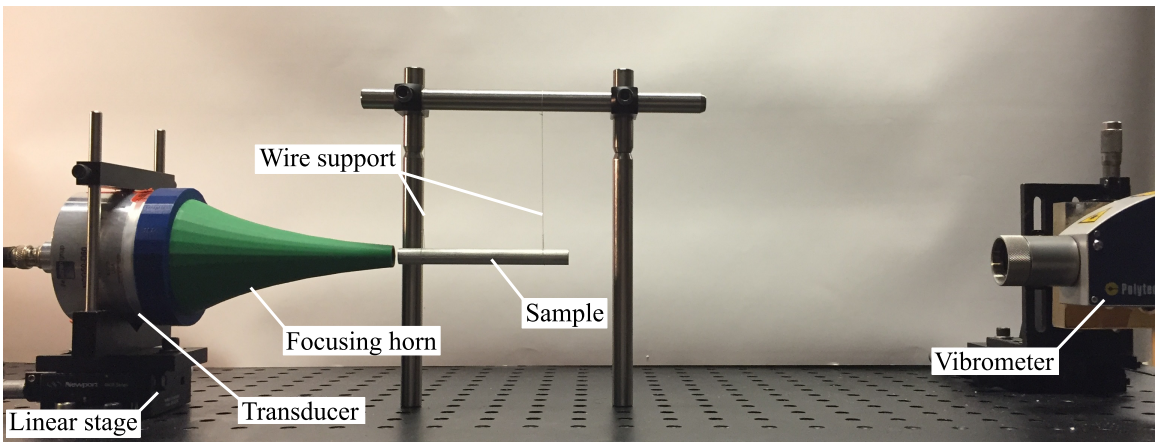

Figure 30: Picture of experimental setup for air-coupled NRUS measurements of rods and bars

Van Den Abeele et al. [29] and Bart Van Damme & Van Den Abeele [31] have used acoustic speakers to excite bending modes of slate and composite beam samples. Bart Van Damme & Van Den Abeele also used a cone to increase sound pressure and detected the motion with a laser vibrometer for applying the nonlinear reverberation spectroscopy (NRS) technique. This method evaluates the frequency-amplitude dependence of the vibration decay after exciting the sample near resonance. With both of these experimental setups it was possible to detect sufficient nonlinear hysteretic behavior for further material damage, but for materials with comparably much stronger hysteretic character than metals and larger defects than precipitates and dislocations, such as micro and fatique cracks.

5.1.1 Samples

For this type of setup slender rod and bar samples are used. The rod samples with a diameter of 9.5 mm, one from stainless steel and one from aluminium, are cut to a length of 100 mm. The bar samples are EDM-cut out of the 17-4PH stainless steel blocks with different heat treatment, introduced in chapter 3, to the dimensions of 10 mm x 10 mm x 100 mm.

5.1.2 Transducer with Acoustic Focusing Horn

For high excitation of the rather small longitudinal eigenfrequencies, a 50 mm Ultran NCG50-D50 noncontact transducer with nominal frequency of 50 kHz is used. The amplifier is set up to amplify the frequency sweep signal up to 125 V, a value close to the tolerable upper limit for constant operation.

Since tests with just the transducer showed no excitation of the samples a focusing horn is used to focus the emitted sound waves onto the comparable small end face of the samples. From Kim [16] a simple design procedure for exponential acoustic horns, based on Webster's horn equation, is used. It relates a gradual change of the

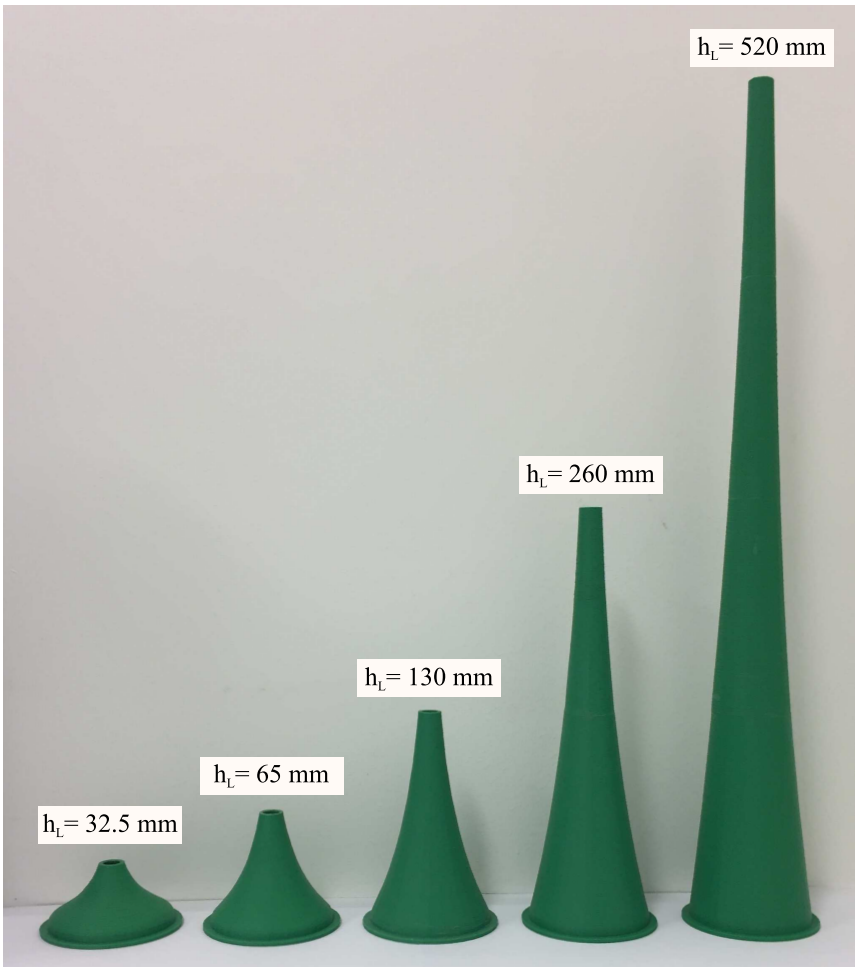

Figure 31: Picture of the used focusing horns

cross-sectional area of the horn to the exponential relationship

$$S = S_t \, e^{k_h x}, \tag{18}$$

where S_t is the cross-sectional area of the throat, the thinner end of the horn, and k_h is the flare constant. The flare constant is defined by the speed of sound in air c_a and the lower cut-off frequency f_c with

$$k_h = \frac{4 \, \pi \, f_c}{c_a}. \tag{19}$$

Below that cut-off frequency the resistance in the throat becomes zero and the horn is described to cut off.

The diameter of mouth and throat of the horn are determined by the geometry of the transducer and the specimens and the cut-off frequency is chosen to be 1800 Hz for a medium sized horn with a length of h_L =130 mm. To narrow down the optimal horn design for maximal sample excitation the medium sized horn and four more horns with shorter and longer lengths are 3D-printed using thermoplastic ABS filament. The length of the produced horns, shown in Figure 31 starts at 32.5 mm and increases by doubling the length with each longer horn up to 520 mm.

5.2 Measurement Procedure and Data Processing

The measurement procedure starts, after making sure that the sample stopped swinging in the wire support, with finding the optimal distance between horn throat and sample. The optimal distance for the highest excitation amplitude is not the closest, instead the excitation amplitude has periodic peaks that are overall decaying with further distance. By varying the horizontal gap width with the linear stage and simultaneously evaluating the time domain signal of the same frequency sweep on the oscilloscope the distance with highest excitation of the time domain signal can be detected. This value alternates for the different horns between approximately 2 mm - 4 mm.

The data processing steps and procedures are similar to those for the NRUS measurements for small plates, described in detail in section 4.2. But instead of introducing a relative nonlinearity parameter, a necessary analytical relationship between the measured velocity v and average volumetric strain ϵ for purely longitudinal deformation to solve equation 3 is given by the derivation of

$$\epsilon = \frac{\partial u_n}{\partial x} \qquad \text{with} \qquad u_n = U cos\left(k_n x\right), \tag{20}$$

where U is the displacement amplitude, to

$$\epsilon = -k_n U sin\left(k_n x\right) = -\frac{2\pi f_n}{c} U sin\left(k_n x\right) \tag{21}$$

with the strain amplitude

$$\Delta\epsilon = \frac{2\pi f_n}{c}\, U. \tag{22}$$

With $v = u\pi f$ and $c = 2fL$ this yields to

$$\Delta\epsilon = \frac{v}{f_n L}. \tag{23}$$

Since the quality factor increased sufficiently for this type of experimental setup (Table 5) and the nonlinear effects appear much smaller, Δf, the frequency bandwidth around the equilibrium resonance frequency $f_0 \pm \Delta f$ is reduced to 0.1 % while the sweep duration is increased to 2 s with a sampling rate of 500 kSa/s. The longer sweeps and shorter frequency bandwidth improve reaching a steady state at each frequency during the sweep and increase numerical accuracy of the FFT while extending the experimental procedure time span potentially elevating temperature influences.

For the previous NRUS measurements with small plates the implemented temperature correction as shown in Figures 18 - 19 improved the R^2-value significantly without substantially influencing the relative nonlinearity parameter. For the NRUS measurements for rods and bars the influence of temperature differences on the final nonlinear parameter, α, is much more drastic. For example, the average difference between the raw and corrected α-value for all the measurements of the stainless steel rod is 33.7 % although installing a simple cardboard box to reduce air fluctuation, but with the temperature correction bringing the average standard deviation of the final corrected α-values overall down to acceptable 2.96 %.

5.3 Modal Analysis

Similar to the proceeding in section 4.3 the longitudinal eigenmode shapes are simulated with the finite element analysis software COMSOL Multiphysics 5.2 and then compared to experimentally gathered long frequency sweeps.

Figure 32 illustrates the displacement and volumetric strain fields of the eigenmodes with longitudinal distortion in free boundary configuration. The illustration

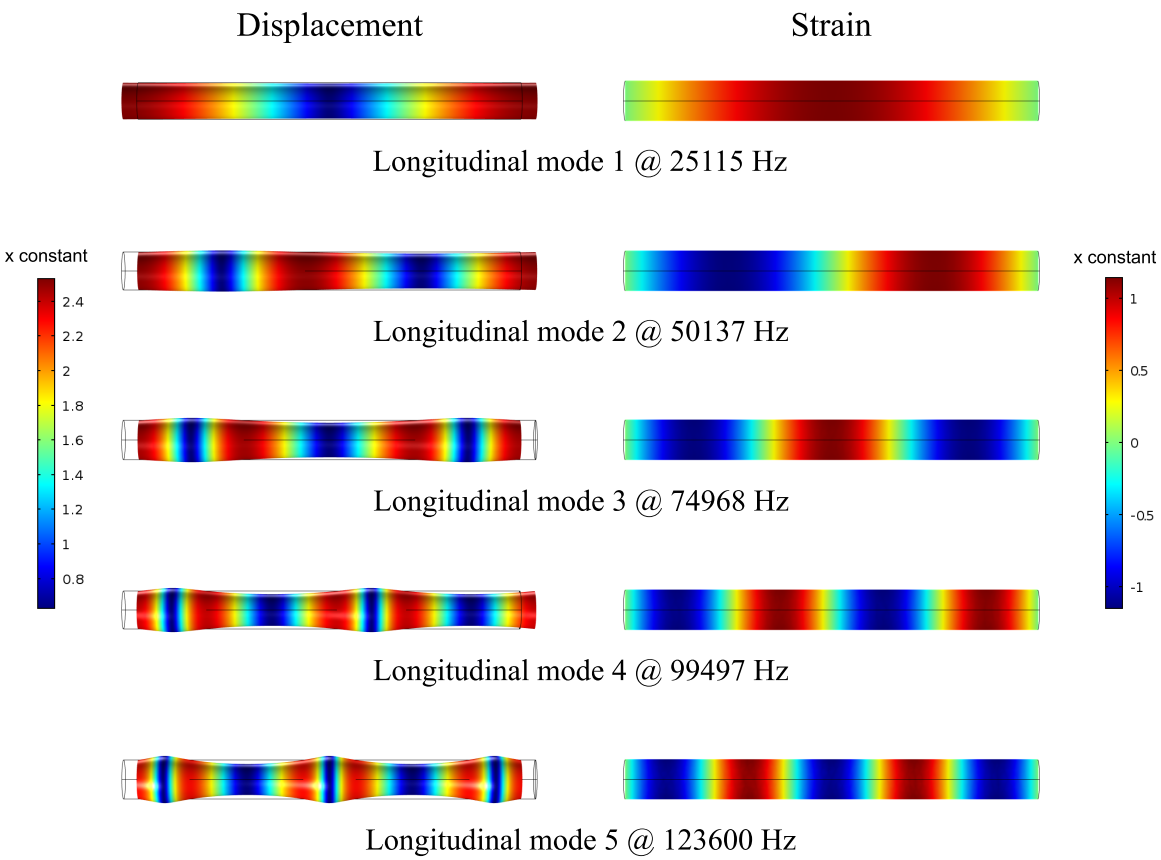

Figure 32: Displacement (left) and volumetric strain fields (right) of the first five longitudinal eigenmodes and corresponding natural frequencies up to 150 kHz of a stainless steel rod in free-free boundary condition

of the volumetric strain field also shows that the zones with positive and negative strain alternate in the rod. Again, the amplitudes for such eigenfrequency studies are arbitrary.

The experimental frequency spectrum of the filtered frequency response of the velocity and associated eigenmode numbers are shown in Figure 33. *Longitudinal mode 2* at 50 157 Hz, the closest to the nominal frequency of the transducer, experiences the highest excitation whereas the amplitudes of the other eigenmodes with increasing frequency difference decay.

The comparison of experiment to simulation in Table 5 demonstrates an even smaller difference than for the analysis for the plates with keeping the maximal aberration under 0.3 %. The procedure was mainly the same, all the material properties

for stainless steel are kept default, only the value of the Young's modulus was reduced to 198.3 MPa to achieve best possible conformance for the first mode.

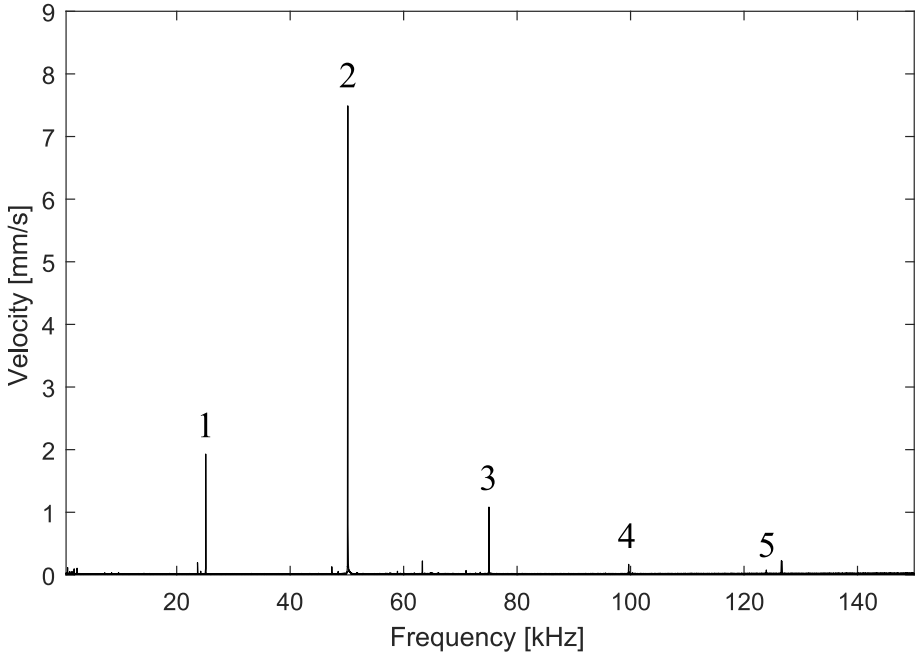

Figure 33: Filtered frequency response of the velocity for the stainless steel rod and denotation of the corresponding longitudinal eigenmodes

Table 5: Comparison of natural frequencies between experiment (f_{exp}) and simulation (f_{sim}) of the stainless steel rod sample

longitudinal mode	f_{exp} [Hz]	f_{sim} [Hz]	$\lvert f_{sim} - f_{exp} \rvert$ [Hz]	$\frac{\lvert f_{sim} - f_{exp} \rvert}{f_{exp}}$	Q_{exp}
1	25114	25115	1	0.003 %	12200
2	50157	50137	20	0.040 %	15600
3	75039	74968	71	0.095 %	16350
4	99666	99497	169	0.170 %	9800
5	123935	123600	335	0.270 %	5600

5.4 System Nonlinearity

The claim from section 4.5 that possible nonlinear behavior of the electric components that are involved in the excitation of the specimen are not influencing the measured nonlinearity also applies for this setup. The transducer that previous research identified as a significant source of undesired nonlinear effects [5] [28] and the prefixed amplifier and function generator are not directly coupled to the specimen. They initiate the vibration, but close to each natural frequency the resonance behavior of the specimen, driven by the natural amplification, enhances this movement multiple times over, fully dictating its motion.

5.5 Comparison of the Focusing Horns

The motivation for comparing different horn lengths is to optimize the achieved strain level in the specimen. For each horn the procedure of finding an optimal distance between throat and rod sample introduced in section 5.2 is carried out and a series of five measurements of *longitudinal mode 2*, the mode with highest excitation level, is performed. The results for maximal achieved strain level and corresponding α-value are compared in Figure 34 and Table 6.

The optimal horn for maximal excitation appears to be the medium sized 130 mm focusing horn, therefore all following measurements are executed with this horn. The comparison also shows that α is apparently dependent on ϵ_{max} with increased measured nonlinearity and improved standard deviation. Evaluation of α for the h_L=130 mm horn measurements for a maximal strain level of only up to 2.2e-6 similar to ϵ_{max} for the h_L=65 mm horn measurements leads to an α-value of -600 (see *-mark in Figure 34) that is similar to the of the h_L=65 mm-horn value.

This phenomenon shows that the nonlinearity parameter is not dependent on the horn itself, but increases with the strain level in the sample. On the basis of each individual plot of the frequency shift these characteristics are hard to see because

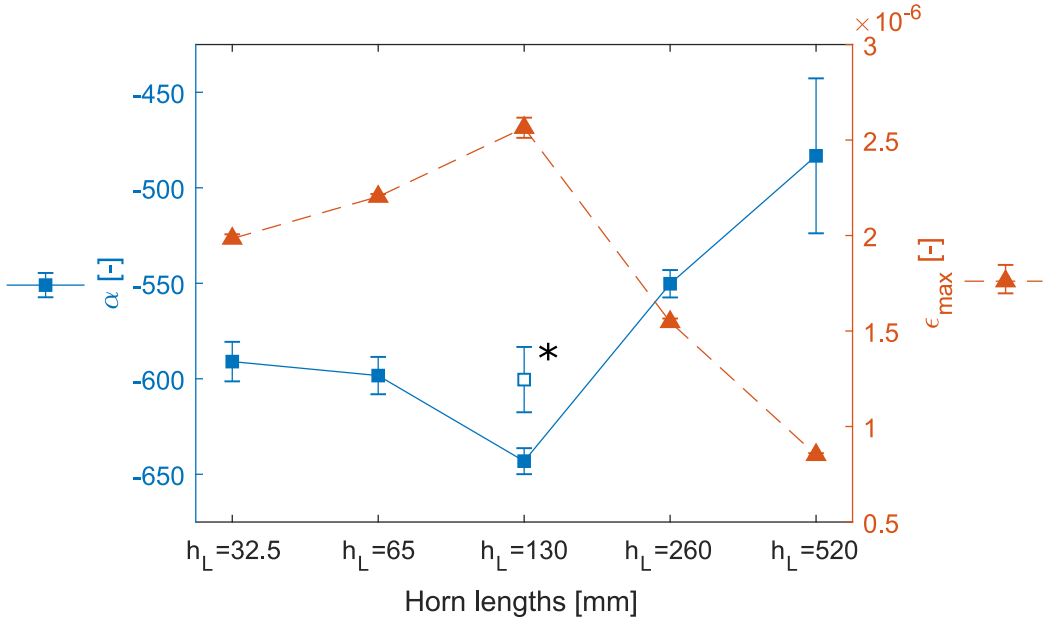

Figure 34: Comparison of measured α-values and achieved maximal strain ϵ_{max} of the stainless steel rod for different horn lengths h_L; *α for evaluation of linear fit up to strain level of 1.4e-6

the single data points are too scattered, but by combining all the data points of the five measurements and fitting a second order polynom, shown in Figure 35, reveals slightly curved behavior.

Table 6: Values of α and ϵ_{max} for different horn lengths h_L

h_L [mm]	ϵ	$\Delta\epsilon/\epsilon_{h_L=32.5}$	α	$\Delta\alpha/\alpha_{h_L=32.5}$
32.5	1.98e-6		-591	
65	2.20e-6	+11.1 %	-593	+0.4 %
130	2.56e-6	+29.2 %	-643	+8.8 %
260	1.55e-6	+22.0 %	-550	-6.9 %
520	0.85e-6	-57.1 %	-483	-18.2 %

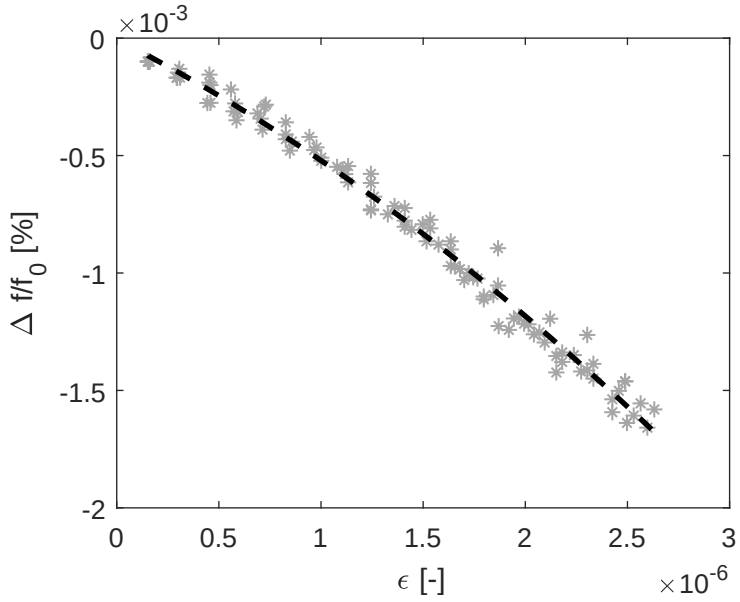

Figure 35: Second order polynomial fit of five measurements of stainless steel rod combined

5.6 Results for Different Eigenmodes and Materials

In Figure 36, a comparison of measurements of the first three longitudinal modes for the aluminium and stainless steel rod is given.

First of all, a clear difference in nonlinear behavior of aluminium to stainless steel can be identified, where aluminium has a very linear character that again corresponds to NRUS measurements from Haupert et al. [13]. Furthermore, the graph shows that measurements of *longitudinal mode 1* result in far-scattered data points and insufficient linear fit while measurements for *longitudinal mode 3* lack in significant excitation of the specimen. Evaluation of *longitudinal mode 2* leads to both adequate excitation and good linear fit and lastly it can be observed that aluminium experiences essentially higher excitation for all the modes.

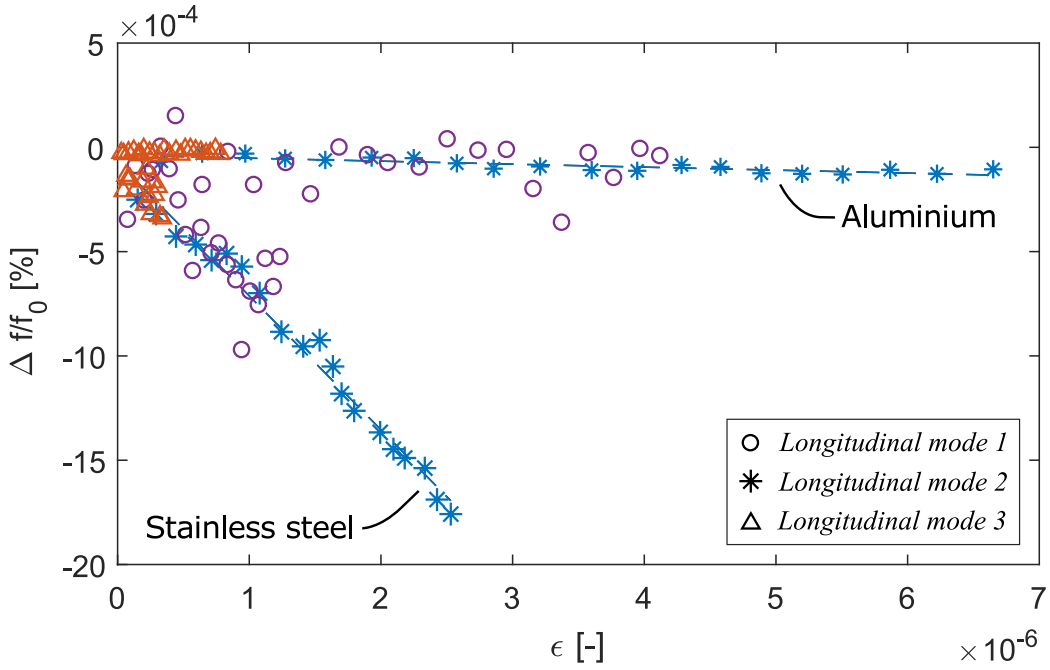

Figure 36: Comparison of stainless steel and aluminium rods for *longitudinal modes 1-3*

This effect can be explained by the coefficient T_l of the longitudinal acoustic wave transmission for the different transmission media pairings

$$T_l = \frac{2\,Z_1}{Z_1 + Z_2} \qquad \text{with} \qquad Z = \rho\, c, \tag{24}$$

where Z is the acoustic impedance. This yields to a transmission coefficient for air to steel of 0.00193 % and an about 2.7 times bigger coefficient for air to aluminium of 0.00521 % that in turn exactly correlates to the gain in excitation.

Table 7: Comparison of stainless steel and aluminium rods for *longitudinal mode 2*

Material	f_0 [Hz]	α	Standard deviation	R^2
Aluminium	50147	-643	1.06 %	0.98
Stainless steel	50844	-12.6	11.6 %	0.71

5.7 Results for Thermally Aged 17-4PH Stainless Steel

The preliminary tests on the aluminium and steel rods helped to understand the influential components and parameters to optimize and validate the experimental setup. Now, the measurement series for thermally aged 17-4PH stainless steel should assess the sensitivity of the NRUS measurements to microstructural changes in steel due to precipitation formation. The used material samples are specimen with bar reference geometry, introduced in Table 2. Each sample is measured ten times.

5.7.1 RUS Results

Below, Figure 37 shows the change in linear resonance frequency f_0 for the different heat treatments. The results indicate a steady increase of resonance frequency for longer aging time with very small deviation for the multiple measurements.

From the analytical description of the n-th natural frequencies $f_n = nc/2L$ (Eq. 16), where the phase speed is $c = \sqrt{E/\rho}$, follows rearranged for the Young's modulus

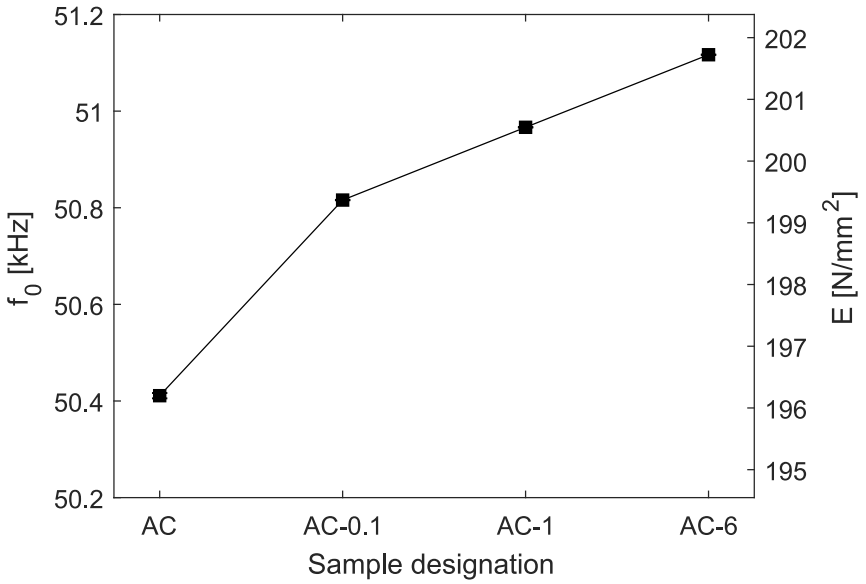

Figure 37: Linear resonance frequency f_0 of thermally aged 17-4PH stainless steel samples and consequential Young's modulus E. It should be noted that because of the quadratic portion of the frequency the E-tick marks are slightly unequally spaced

Table 8: RUS results with derived Young's modulus E of thermally aged 17-4PH stainless steel samples

Sample condition	f_0 [Hz]	$\Delta f_0/f_{0,AC}$	Standard deviation	E [N/mm^2]	$\Delta E/E_{AC}$
AC	50411		0.0109 %	196.2	
AC-0.1	50815	+0.80 %	0.0008 %	199.4	+1.61 %
AC-1	50967	+1.10 %	0.0013 %	200.5	+2.22 %
AC-6	51117	+1.40 %	0.0008 %	201.7	+2.82 %

and the second longitudinal eigenmode $E = (f_2 L)^2 \rho$. This allows determining the Young's modulus from the resonance frequency and shows consequential a steady stiffness gain of up to 2.82 % for an aging time of 6 h (Table 8).

These results indicate that the formed copper-rich precipitates that are stiffer than the Fe-matrix reinforce the matrix, leading to an increased stiffness. Rosen et al. [27] also noted an increase in stiffness for proceeding precipitation formation in aluminium alloy 2219.

5.7.2 NRUS Results

Figure 38 and Table 9 give the hysteretic nonlinearity parameter, α, averaged for ten measurements. The R^2-values, characterizing the linear fit for each individual measurement, indicate moderate linear approximation for less nonlinear behavior and compared to the linear RUS measurements the error bars are considerably larger, but for the given mean values a clear trend is still identifiable.

With longer aging time the nonlinear behavior intensifies noticeably by more negative α-values (or higher abs(α)-values). The trend also shows a decreasing gain in nonlinearity for each consecutive aging time step, almost leveling off between 1 h and 6 h. While abs(α) increases overall by 89 % the increase of 1 h aging to 6 h is only 1.51 %.

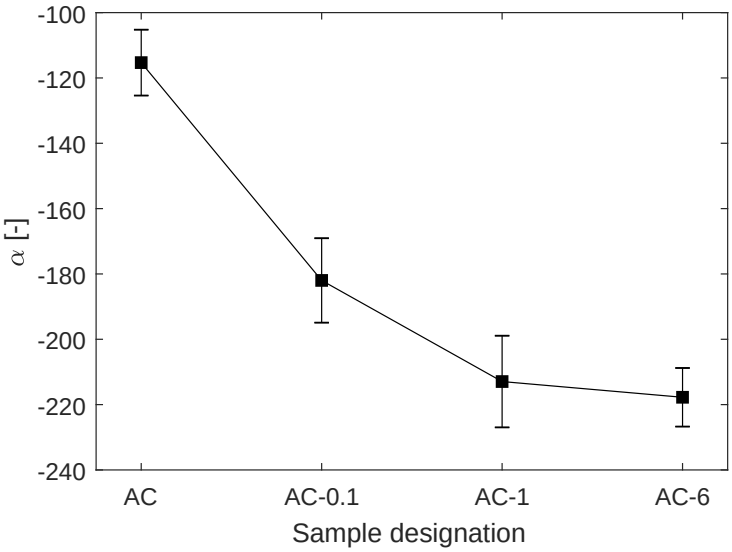

Figure 38: Hysteretic nonlinearity parameter, α, of thermally aged 17-4PH stainless steel samples

As discussed in section 2.1, nonlinear behavior of materials of the atomic-elasticity class currently lack in theoretical models describing nonlinear elastic hysteretic effects on an atomic scale. On a mesoscopic level hysteresis is traced to softer regions in a hard material like soft bonding regions between grain boundaries or microcracks and pores [1]. The nonlinear hysteretic behavior observed here in this case due to precipitation formation is most likely based on a dislocation-precipitation interaction.

Table 9: NRUS results of thermally aged 17-4PH stainless steel samples

Sample condition	abs(α)	$\Delta\alpha/\alpha_{AC}$	Standard deviation	R^2
AC	73.4		8.74 %	0.67
AC-0.1	115.0	+56.6 %	6.60 %	0.78
AC-1	136.6	+86.0 %	8.93 %	0.92
AC-6	138.6	+88.9 %	5.71 %	0.91

5.7.3 Comparison with other Monitoring Techniques

The results for the linear resonance frequency and consequential conclusion of increasing stiffness of the material samples for longer thermal aging agree very well with the hardening measurements from section 3.3.1 as shown in Figure 39. Both techniques show pretty much a linear relation to thermal aging time consistent with the assumption of continuous precipitation formation throughout the heat treatment.

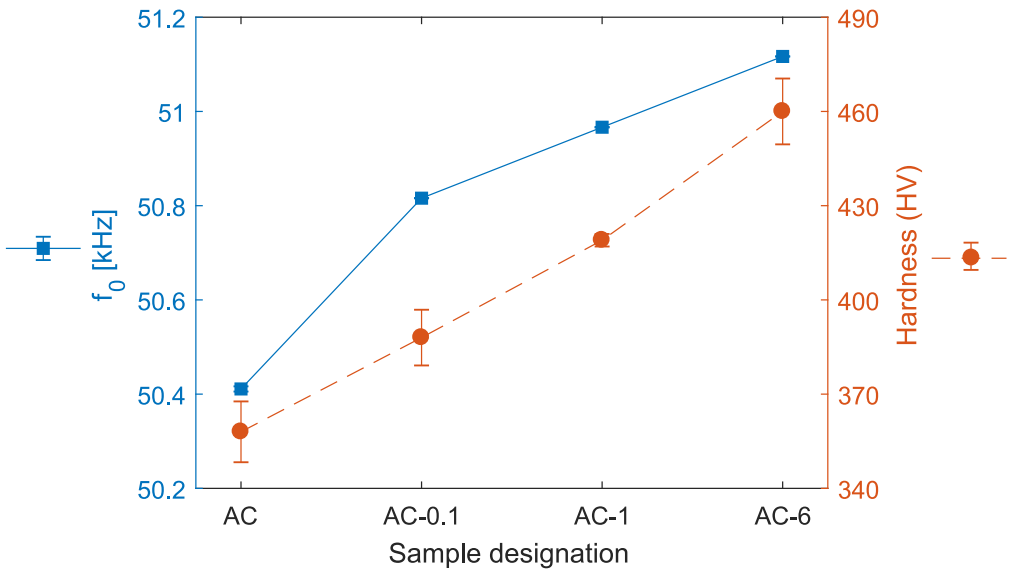

Figure 39: Comparison of measurements of linear resonance frequency f_0 to Vickers hardness measurements from Thiele [28]

A comparison of normalized values of α, β', Vickers hardness and TEP is given in Figure 40. The α-measurements reflect more the development of the TEP-value, that also shows slightly flattening increase for the 6 h aging (see also Figure 10) while the relative β' nonlinearity measurements show consecutive steady decrease with a bigger decline between 0.1 h and 1 h (see also Figure 11). Vickers hardness and TEP measurements both provide indirectly evidence of increasing precipitation formation for longer times of thermal aging. Matlack et al. [19] traced the decrease of the relative acoustic nonlinearity parameter, β', for increasing times of thermal aging at 400°C to

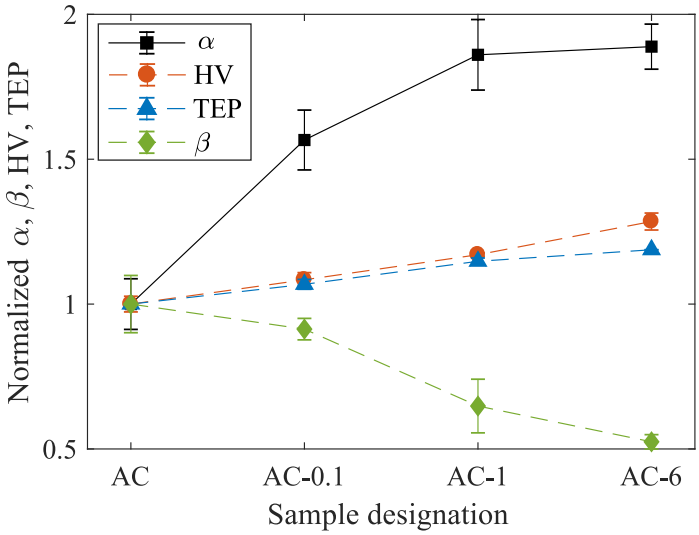

Figure 40: Comparison of normalized α to normalized relative β', Vickers hardness and TEP-measurements from Matlack [19] and Thiele [28]

the precipitate-pinned dislocation contribution, the radius of the precipitates and the number of precipitates. Assuming constant average radius of the precipitates during the heat treatment, they related the decrease of the acoustic nonlinearity parameter proportionally to the increase in hardness for further thermal aging.

Compared to these complementary measurements the α parameter shows great sensitivity to the applied thermal damage, as Table 10 points out.

Table 10: Comparison of material properties and parameters from RUS and NRUS techniques to complementary measurement techniques in respect to sensitivity to applied thermal damage

Measurement technique	Material property /parameter	Sensitivity ΔAC-6/AC
RUS	E	+2.8 %
NRUS	α	+89 %
Vickers hardness	HV	+28 %
Thermo-electric power	TEP	+19 %
Rayleigh surface waves	β	-47 %

CHAPTER VI

CONCLUSION AND OUTLOOK

6.1 Conclusion for NRUS for Small Plates

The steps provided in chapter 4 show that the NRUS setup for small plates is capable of exciting the various eigenmodes of the specimen and measuring their natural frequencies with good conformance to a linear finite element eigenfrequency analysis. It has also been shown that the recording of increasing excitation amplitudes and resonance frequency with this setup and the involved data processing steps is accurate enough to determine a shift in resonance frequency. Further steps improved the influence of ambient temperature changes on the nonlinear measurements and identified the contact conditions between sample to steel base and transducer as source of additional unwanted nonlinearity based both on simulation and experimental results.

Although many influential parameters such as the contact force were chosen in a way to reduce negative influence to the measurements and effort was put in to keep these factors constant for the individual measurements, it was not possible to show sufficient sensitivity to microstructural changes in heat-treated 17-4PH stainless steel. Most likely the nonlinearity due to the influence of the contact conditions overlay with the actual material nonlinearity in such a considerable extent that the material nonlinearity gets lost in it.

Further evaluation of the achieved strain level in the sample through solving the time-dependent solution for a forced vibration with the FEM model and matching the displacement amplitude with the experiment showed that the maximal strain amplitude of approximately 1e-6 is very small compared to other research. This and the fact that it was not possible to develop an analytical velocity and strain

relationship, needed to determine absolute α, would limit the method anyway.

6.2 Conclusion for NRUS for Rods and Bars

On the basis of the gained experiences with the contact excitation measurements a fully noncontact setup for rods and bars was developed. The excitation of the samples with the air-coupled transducer, paired with an optimized focusing horn, proved strong enough to excite the first five eigenmodes and to determine the corresponding resonance frequency with very high quality factors and very good correspondence to an FEM simulation, indicating low damping and small influencing factors. The NRUS measurements finally lead to an absolute determination of the hysteretic nonlinearity parameter, α, with the temperature correction, introduced in chapter 4, turning out to be crucial for accurately repeatable measurements.

The comparison of aluminium and stainless steel rods showed agreement with other research, demonstrated performance characteristics of the different longitudinal eigenmodes in combination with the used experiment components and revealed a slightly curved frequency shift.

With the linear RUS measurements for the thermally aged 17-4PH stainless steel it was possible to determine the Young's modulus with very small mean variation, demonstrating significant influence of the heat treatment to the stiffness of the material. The NRUS measurements for the thermally aged stainless steel samples identified a clear trend of increasing nonlinear behavior for further heat treatment with showing great sensibility to the microstructural changes compared to complementary measurements of Vickers hardness, thermo-electric power and β-nonlinearity.

This NRUS measurement setup finally achieved the set goals by providing a reliable, accurate and valid method to measure the hysteretic nonlinearity parameter. Due to the absence of operator-dependent process steps, a highly automated measurement procedure and minimal sample preparation the individual measurements

are accurately repeatable and fast such that extensive material studies are well feasible.

6.3 Outlook

The proposed noncontact excitation setup allows fast and reliable future analysis of microstructural changes in metallic specimen for example due to deformation, temperature and pressure fluctuations, creep, fatigue and nuclear irradiation. The analysis of other materials is also conceivable insofar the impedance properties allow sufficient energy transmission and therefore adequate excitation.

Of course, the setup can be further improved by using stronger transducers in combination with focusing horns that are further optimized in dimensions and shape. Matching the sample's natural frequency of the first longitudinal eigenmode to the nominal frequency of the transducer by varying the length of the sample could also further improve the achievable excitation levels. To increase the accuracy of the measurements by reducing the temperature influence, a climate chamber or any kind of temperature stabilization will also improve the measurements, especially for the investigation of very small strain levels.

REFERENCES

[1] Barsoum, M. W., Radovic, M., Zhen, T., Finkel, P., and Kalidindi, S. R., "Dynamic elastic hysteretic solids and dislocations," *Physical review letters*, vol. 94, no. 8, p. 085501, 2005.

[2] Burgos, D., Mujica, L., and Rodellar, J., *Emerging Design Solutions in Structural Health Monitoring Systems*. Advances in civil and industrial engineering (ACIE) book series, Engineering Science Reference, 2015.

[3] Chen, J., Kim, J.-Y., Kurtis, K. E., and Jacobs, L. J., "Theoretical and experimental study of the nonlinear resonance vibration of cementitious materials with an application to damage characterization," *The Journal of the Acoustical Society of America*, vol. 130, no. 5, pp. 2728–2737, 2011.

[4] COMSOL Multiphysics 5.2a Tutorial, "Various analyses of an elbow bracket." `https://www.comsol.com/model/various-analyses-of-an-elbow-bracket-4131`. [Online; accessed 05-30-2017].

[5] Ehrlich, C., "Experimental characterization of creep damage using the nonlinearity ultrasonic technique," Master's thesis, Georgia Institute of Technology, Atlanta, GA, USA, 8 2011.

[6] Ensminger, D., *Ultrasonics: Fundamentals, Technology, Applications, Second Edition, Revised and Expanded*. Dekker Mechanical Engineering, Taylor & Francis, 1988.

[7] Finkel, P., Zhou, A. G., Basu, S., Yeheskel, O., and Barsoum, M. W., "Direct observation of nonlinear acoustoelastic hysteresis in kinking nonlinear elastic solids," *Applied Physics Letters*, vol. 94, no. 24, p. 241904, 2009.

[8] Forstenhäusler, M., "Nonlinear resonance ultrasonic spectroscopy for characterizing thermal damage in 17-4ph stainless steel," Master's thesis, Georgia Institute of Technology, Atlanta, GA, USA, 8 2016.

[9] Gliozzi, A. S., Nobili, M., and Scalerandi, M., "Modelling localized nonlinear damage and analysis of its influence on resonance frequencies," *Journal of Physics D: Applied Physics*, vol. 39, no. 17, p. 3895, 2006.

[10] Granato, A. and Lücke, K., "Theory of mechanical damping due to dislocations," *Journal of Applied Physics*, vol. 27, no. 6, pp. 583–593, 1956.

[11] Guyer, R. A. and Johnson, P. A., "Nonlinear mesoscopic elasticity: Evidence for a new class of materials," *Physics Today*, vol. 52, pp. 30–36, Apr. 1999.

[12] Haoqi Li, F. R., "Resonant ultrasound spectroscopy offers unique advantages as a nondestructive test method," *Advanced Materials and Processes*, vol. 172, no. 10, pp. 17–19, 2014.

[13] Haupert, S., Renaud, G., Riviere, J., Talmant, M., Johnson, P. A., and Laugier, P., "High-accuracy acoustic detection of nonclassical component of material nonlinearity," *The Journal of the Acoustical Society of America*, vol. 130, no. 5, pp. 2654–2661, 2011.

[14] Hsu, K.-C. and Lin, C.-K., "High-temperature fatigue crack growth behavior of 17-4PH stainless steels," *Metallurgical and Materials Transactions A*, vol. 35, no. 9, pp. 3018–3024, 2004.

[15] Jhang, K.-Y., "Nonlinear ultrasonic techniques for nondestructive assessment of micro damage in material: A review," *International Journal of Precision Engineering and Manufacturing*, vol. 10, no. 1, pp. 123–135, 2009.

[16] Kim, Y., *Sound Propagation: An Impedance Based Approach*. John Wiley and Sons, Ltd, July 2010.

[17] Kinsler, L. E., *Fundamentals of acoustics*. Wiley, 1982.

[18] Matlack, K., *Nonlinear Ultrasound for Radiation Damage Detection*. PhD thesis, Georgia Institute of Technology, Atlanta, GA, USA, 5 2014.

[19] Matlack, K. H., Bradley, H. A., Thiele, S., Kim, J.-Y., Wall, J. J., Jung, H. J., Qu, J., and Jacobs, L. J., "Nonlinear ultrasonic characterization of precipitation in 17-4ph stainless steel," *NDT & E International*, vol. 71, pp. 8–15, 2015.

[20] Matlack, K., Kim, J.-Y., Jacobs, L., and Qu, J., "Review of second harmonic generation measurement techniques for material state determination in metals," *Journal of Nondestructive Evaluation*, vol. 34, no. 1, p. 273, 2015.

[21] Mirzadeh, H. and Najafizadeh, A., "Aging kinetics of 17-4PH stainless steel," *Materials chemistry and physics*, vol. 116, no. 1, pp. 119–124, 2009.

[22] Murayama, M., Hono, K., and Katayama, Y., "Microstructural evolution in a 17-4PH stainless steel after aging at 400 °C," *Metallurgical and Materials Transactions A*, vol. 30, no. 2, pp. 345–353, 1999.

[23] Northwood, D. O., Sun, X., Hochreiter, J., Sokolowski, J. H., and Penrod, D. E., "Thermoelectric power (TEP) measurements as a materials characterization technique," *AIP Conference Proceedings*, vol. 316, no. 1, pp. 181–184, 1994.

[24] Ohtani, T., Kusanagi, Y., and Ishii, Y., "Noncontact nonlinear resonant ultrasound spectroscopy to evaluate creep damage in an austenitic stainless steel," *AIP Conference Proceedings*, vol. 1511, no. 1, pp. 1227–1233, 2013.

[25] Payan, C., Ulrich, T. J., Bas, P. Y. L., Saleh, T., and Guimaraes, M., "Quantitative linear and nonlinear resonance inspection techniques and analysis for material characterization: Application to concrete thermal damage," *The Journal of the Acoustical Society of America*, vol. 136, no. 2, pp. 537–546, 2014.

[26] Rana, R., Singh, S., and Mohanty, O., "Thermoelectric power studies of copper precipitation in a new interstitial-free steel," *Scripta Materialia*, vol. 55, no. 12, pp. 1107 – 1110, 2006.

[27] Rosen, M., Horowitz, E., Fick, S., Reno, R., and Mehrabian, R., "An investigation of the precipitation-hardening process in aluminum alloy 2219 by means of sound wave velocity and ultrasonic attenuation," *Materials Science and Engineering*, vol. 53, no. 2, pp. 163 – 177, 1982.

[28] Thiele, S., "Air-coupled detections of rayleigh surface waves to assess material nonlinearity due to precipitation in alloy steel," Master's thesis, Georgia Institute of Technology, Atlanta, GA, USA, 8 2013.

[29] Van Damme, B. and Van Den Abeele, K., "The application of nonlinear reverberation spectroscopy for the detection of localized fatigue damage," *Journal of Nondestructive Evaluation*, vol. 33, pp. 263–268, Jun 2014.

[30] Van Den Abeele, K. E. and Johnson, P. A.and Sutin, A., "Nonlinear elastic wave spectroscopy (NEWS) techniques to discern material damage. Part I: Nonlinear wave modulation spectroscopy (NWMS)," *Research in Nondestructive Evaluation*, vol. 12, no. 1, pp. 17–30, 2000.

[31] Van Den Abeele, K., Carmeliet, J., Ten Cate, J., and Johnson, P., "Nonlinear elastic wave spectroscopy (NEWS) techniques to discern material damage, Part II: Single-mode nonlinear resonance acoustic spectroscopy," *Research on Nondestructive Evaluation*, vol. 12, no. 1, pp. 31–42, 2000.

[32] Windels, F. and Abeele, K. V. D., "The influence of localized damage in a sample on its resonance spectrum," *Ultrasonics*, vol. 42, no. 1, pp. 1025 – 1029, 2004. Proceedings of Ultrasonics International 2003.